TITLE

***Let-7* restrains an oncogenic circuit in AT2 cells to prevent fibrogenic cell intermediates in pulmonary fibrosis.**

AUTHORS

Matthew J. Seasock[1,2,], Md Shafiquzzaman[2,], Maria E. Ruiz-Echartea[3], Rupa S. Kanchi[3,4], Brandon T. Tran[5,6], Lukas M. Simon[7], Matthew D. Meyer[8], Phillip A. Erice[1,2], Shivani L. Lotlikar[2], Stephanie C. Wenlock[9], Scott A. Ochsner[3], Anton Enright[9], Alex F. Carisey[10,13], Freddy Romero[11,14], Ivan O. Rosas[11], Katherine Y. King[6], Neil J. McKenna[3], Cristian Coarfa[3,4], Antony Rodriguez[2,4,12,*]

[1]Immunology & Microbiology Graduate Program, Baylor College of Medicine, Houston, TX, 77030.

[2]Department of Medicine, Section of Immunology, Allergy & Rheumatology, Baylor College of Medicine Houston TX, 77030.

[3]Department of Molecular and Cellular Biology, Baylor College of Medicine, Houston, TX, 77030.

[4]Dan L. Duncan Comprehensive Cancer Center, Baylor College of Medicine Houston, TX, 77030.

[5]Graduate Program of Cancer Biology and Cell Biology, Baylor College of Medicine, Houston, TX, 77030.

[6]Department of Pediatrics, Division of Infectious Diseases, Texas Children's Hospital, Baylor College of Medicine, Houston, TX, 77030.

[7]Therapeutic Innovation Center, Baylor College of Medicine, Houston, TX, 77030.

[8]Shared Equipment Authority, Rice University, Houston, TX 77005.

[9]Department of Pathology, University of Cambridge, Cambridge, CB2 1TN, UK

[10]William T. Shearer Center for Immunobiology, Texas Children's Hospital, Houston, TX, 77030.

[11]Department of Medicine, Section of Pulmonary and Critical Care, Baylor College of Medicine. Houston, TX, 77030.

[12]Center for Translational Research on Inflammatory Diseases, Michael E. Debakey, Baylor College of Medicine, Houston, TX, 77030.

[13]Current Address: Department of Cell and Molecular Biology, St. Jude Children's Research Hospital, Memphis, TN

[14]Current Address: Vertex Pharmaceuticals, 3215 Merryfield Row, San Diego, CA, 92121.

These authors contributed equally: Matthew J. Seasock, Md Shafiquzzaman
Author Correspondence: antonyr@bcm.edu

ABSTRACT

Analysis of lung alveolar type 2 (AT2) progenitor stem cells has highlighted fundamental mechanisms that direct their differentiation into alveolar type 1 cells (AT1s) in lung repair and disease. However, microRNA (miRNA) mediated post-transcriptional mechanisms which govern this nexus remain understudied. We show here that the *let-7* miRNA family serves a homeostatic role in governance of AT2 quiescence, specifically by preventing the uncontrolled accumulation of AT2 transitional cells and by promoting AT1 differentiation. Using mice and organoid models, we demonstrate genetic ablation of *let-7a1/let-7f1/let-7d* cluster (*let-7afd*) in AT2 cells prevents AT1 differentiation and results in accumulation of AT2 transitional cells in progressive pulmonary fibrosis. Integration of AGO2-eCLIP with RNA-sequencing from AT2 cells uncovered the induction of direct targets of *let-7* in an oncogene feed-forward regulatory network including BACH1/EZH2/MYC which drives an aberrant fibrotic cascade. Additional analyses using CUT&RUN-sequencing revealed an epigenetic role of *let-7* in induction of chromatin histone acetylation and methylation and maladaptive AT2 cell reprogramming. This study identifies *let-7* as a key gatekeeper of post-transcriptional and epigenetic chromatin signals to prevent AT2-driven pulmonary fibrosis.

INTRODUCTION

Lung respiratory diseases rank as major global health challenges and are among the leading causes of death worldwide. Lung regeneration after injury is facilitated by epithelial progenitor stem cells (PSC)s found in airway and alveolar regions[1-3]. These cells are increasingly recognized as crucial factors in the onset of human lung diseases. Interstitial lung diseases (ILD)s are respiratory disorders characterized by excessive accumulation of extracellular matrix (ECM) and fibrotic tissue in alveoli leading to respiratory failure[4]. This condition is linked to abnormalities

61 in facultative epithelial PSCs, especially alveolar type 2 (AT2) cells[5,6]. AT2 cells are crucial for
62 lung alveolar tissue repair, serving dual roles: as PSCs that can differentiate into alveolar type 1
63 (AT1) cells and as homeostatic cells (hAT2) essential for surfactant production[7-9]. Recent studies
64 in some lung injury models found that hAT2 cells become primed (pAT2), self-renew and give rise
65 to heterogeneous population of KRT8^{+} transitional cells (hereafter referred to as ADI, alveolar
66 differentiation intermediates) which can become AT1s[10-13]. Studies have shown that ADIs are
67 characterized by the activation of P53, TGFβ, EMT signaling pathways and their pathological
68 accumulation promotes lung injury and fibrosis[10-13]. A study identified a murine ADI cluster 7
69 subset (ADI-7) associated with stalled AT1 differentiation[13]. In the lungs of patients with Idiopathic
70 Pulmonary Fibrosis (IPF), the most common endotype of ILDs, fibrogenic cells resembling murine
71 ADIs -termed "aberrant basaloid" (AB) cells- persist and appear impaired in AT1-
72 transdifferentiation[11-14].

73 Studies in human IPF tissues and animal models have shown reduced expression of *let-*
74 *7* microRNA (miRNA) family members[15,16], as well as TGFβ/SMAD3 mediated repression of *let-*
75 *7d* in epithelial cells [15]. Systemic inhibition of *let-7* function with an antagomiR was found to trigger
76 thickening of alveolar septa and remodeling[15]. *Let-7* is recognized as a tumor suppressor which
77 prevents the proliferation and metastasis of cancer stem cells via unrestrained induction of
78 multiway hub oncogenes such as EZH2, MYC, and KRAS[17-20]. Also, *let-7* has been shown to act
79 as an orchestrator of key pathways and processes involved in pulmonary fibrosis, including
80 PI3K/AKT/MTOR and epithelial mesenchymal transition (EMT)[20,21].

81 This study delves into the molecular and cellular roles of the *let-7* family in AT2s,
82 underscoring its vital role in lung tissue homeostasis, protection against injury, and fibrosis. We
83 revealed the crucial role of *let-7* as a molecular brake to uncontrolled expansion, activation of AT2
84 PSCs and formation of ADIs. Loss of *let-7* activity in AT2s also hampers cell fate where ADIs are
85 prevented from transitioning into AT1s. Mechanistic studies highlight *let-7* as a gatekeeper of
86 physiologic expression levels of a profibrotic oncogene gene regulatory network (OGRN)

87 comprised of BACH1 [22], EZH2 [23], and MYC [24] in preservation of AT2 cell plasticity and lung
88 homeostasis. Overall, our studies highlight a new dimension for *let-7* as a potent regulator in
89 alveolar stem cell fate and epigenetic perturbations in pulmonary fibrosis.
90

91 **RESULTS**

92 **Time-dependent downregulation of *let-7* family expression during peak formation of ADIs**
93 **after bleomycin-induced lung injury**

94 We examined *let-7* expression dynamics after bleomycin-induced lung injury in mice
95 (GSE195773)[25]. Our analysis of this published small RNA-seq dataset revealed transient
96 downregulation of *let-7* family members at 7- and 14-days relative to controls followed by return
97 to baseline by 21-days post-bleomycin (Supplementary Fig. 1a). Total *let-7* activity decreased
98 approximately 25% after 7-days post-bleomycin in lungs of mice vs controls (Supplementary Fig.
99 1b). Approximately 75% of total activity was comprised from members: *let-7a*, *let-7b*, *let-7c*, *let-*
100 *7d*, and *let-7f*. These *let-7* members are transcribed, in part, from conserved *let-7b/let-7c2* (*let-*
101 *7bc2*) and *let-7a1/let-7f1/let-7d* (*let-7afd*) gene clusters[26] and contribute upwards of 20% and 55%
102 respectively of total *let-7* activity in naive lung (Supplementary Fig. 1b,c). The temporal
103 downregulation of *let-7* expression coincides with the transient appearance and peak formation
104 of injury associated KRT8^{+} ADIs following bleomycin injury[11,12]. Based on these observations, we
105 hypothesized that *let-7* family governs ADI cell formation in alveolar regeneration.
106

107 **Depletion of *let-7afd* in AT2 cells causes spontaneous lung injury acutely**

108 To understand the mechanism of *let-7* function in AT2 cells, we utilized our *let-7bc2* and
109 *let-7afd* conditional knockout (KO) mice[26]. We employed *let-7bc2*$^{f/f}$;*Sftpc-Cre*$^{ERT2/+}$, *let-*
110 *7afd*$^{f/f}$*;Sftpc-Cre*$^{ERT2/+}$ mice with and without the *R26R-LSL-tdTomato* reporter (*Sftpc-tdT*) for
111 phenotypic analysis – hereafter referred to as *let-7bc2*^{AT2} and *let-7afd*^{AT2} mice (Supplementary
112 Fig. 1c). Quantitative RT-PCR (qPCR) from flow sorted *Sftpc-tdT*$^{+}$ AT2 cells confirmed >90%

113 excision of *let-7bc2* or *let-7afd* clusters after intraperitoneal tamoxifen administration (iTAM)
114 (Supplementary Fig. 1d,e).

115 To assess the consequence of deletion of *let-7bc*2 or *let-7afd* clusters, lung histology and
116 physiologic phenotypic analysis were carried out following 6-days of iTAM. Genetic loss of *let-*
117 *7afd* in AT2 cells led to decreased arterial oxygen saturation (SpO2) following iTAM (Fig. 1a).
118 Approximately 28% of *let-7afd*^{AT2} mice developed a pulmonary hemorrhage phenotype discerned
119 by gross lung dissections and hematoxylin and eosin (H&E) stained sections (Fig. 1b,c). The
120 histologic analysis of *let-7afd*^{AT2} mice revealed diffuse bleeding into the alveolar spaces and
121 immune cell infiltration relative to controls (Fig 1c). The *let-7bc2*^{AT2} mice exhibited a milder
122 temporal drop in SpO2 relative to *let-7afd*^{AT2} mice but no hemorrhage phenotype (Fig. 1a,
123 Supplementary Fig. 1f).

124

125 **Deletion of *let-7afd* in AT2 cells stimulates progenitor stem cell proliferation and formation**
126 **of ADI cells acutely in the lung**

127 We performed bulk RNA sequencing (RNA-seq) of whole-lung or flow cytometric sorting
128 of *Sftpc-tdT*$^{+}$ AT2s respectively between *let-7afd*^{AT2} and controls following 6-days of iTAM. Gene
129 set enrichment analysis (GSEA) showed significant induction of cell cycle related genes (*e.g.*,
130 *Mki67*), pAT2 (*e.g.*, *Hif1a*) and ADI/ADI-7 (*e.g., Cldn4, Ctgf)* identity genes upon deletion of *let-*
131 *7afd* in lungs and purified AT2s (Fig. 1d,e,f, Supplementary Fig. 2a,b,c). Lungs and purified AT2
132 cells from *let-7afd*^{AT2} mice also exhibit downregulation of hAT2 markers (Supplementary Fig
133 2a,b,c). Deletion of *let-7afd* led to downregulation of AT1 identity genes in sorted AT2s
134 (Supplementary Fig. 2b). We additionally confirmed increased cycling AT2 lineage cells in lungs
135 of *let-7afd*^{AT2} mice following 14-days of iTAM by immunofluorescence (IF) detection of nuclear
136 KI67 in SFTPC^{+} *Sftpc-tdT*$^{+}$ cells (Fig. 1g,h).

137 To determine if transcriptomic changes arise, in part, due to intrinsic phenotypic changes
138 in AT2 cells, we carried out colony forming efficiency (CFE) measurements in combination with

139 bulk RNA-seq on *let-7afd*^{AT2} and control AT2 cell-derived organoids grown in AT2 maintenance
140 medium (AMM)[27] (Fig. 1i). CFE and spheroid diameters were significantly increased in *let-7afd*^{AT2}
141 cells (Fig. 1j, k, Supplementary Fig. 2d). GSEA and gene ontology (GO) biological process
142 enrichment analysis respectively revealed a striking parallel between *let-7afd*^{AT2} organoids and
143 *Sftpc-tdT* RNA-seq datasets in the induction cell cycle genes (Fig. 1l, Supplementary Fig. 2e).
144 The *let-7afd*^{AT2} organoids exhibited upregulation of pAT2 and ADI markers (Supplementary Fig.
145 2e). However, in contrast with sorted *let-7afd*$^{-/-}$ AT2 cells where hAT2 and AT1 markers appeared
146 repressed, cultured *let-7afd*$^{-/-}$ AT2 organoids maintain similar marker expression as compared to
147 controls (Supplementary Fig. 2e,f). The *let-7afd*$^{-/-}$ organoids did not exhibit significant induction of
148 basal cell identity markers suggesting they are not redirected towards airway cell fate
149 (Supplementary Fig. 2f). Collectively, this data indicates that acute loss of *let-7afd* expression
150 triggers the uncontrolled proliferative expansion of AT2 PSCs and the formation of ADI cells in
151 injured lungs acutely.
152

153 **Integrated biochemical and transcriptomics analysis in the generation of a *let-7* mRNA**
154 **targetome in AT2 cells**

155 To validate and identify functional targets of *let-7*, we performed enhanced Argonaute 2
156 UV-cross-linking immunoprecipitation-sequencing with enrichment of *let-7* targets (AGO2-
157 eCLIP+let-7)[28] in WT mice following 6-days of bleomycin injury (Fig. 2a). The libraries yielded
158 13,027 chimeric *let-7*:mRNA called peaks in the 3'untranslated region (3'UTR) of genes (Fig. 2b,
159 Supplementary Data 1). Motif analysis further showed highly significant and specific enrichment
160 of *let-7* "seed" region binding motifs within chimeric *let-7* peaks (Fig. 2c). Collapsing of chimeric
161 *let-7* peaks into individual transcription units yielded 2009 target genes in acute bleomycin-injured
162 lungs (Fig. 2d).

163 To enrich for functional targets of *let-7* in AT2 cells, we integrated the AGO2-eCLIP+let-7
164 targetome with the sorted *Sftpc-tdT*$^{+}$ and/or organoid transcriptome datasets. Initially, we applied

165 Sylamer [29] on *let-7afd*$^{-/-}$ transcriptome data to ascertain *let-7* post-transcriptionally represses
166 mRNA targets. Sylamer showed prominent miR-mediated mRNA destabilization since the motifs
167 corresponding to *let-7* were enriched within the 3'UTRs of induced genes in *let-7afd*$^{-/-}$ *Sftpc-tdT*$^{+}$
168 cells compared to controls (Fig. 2e). Next, we made use of Venn Diagram intersection analysis to
169 select biochemically validated, significantly upregulated, and experimentally validated *let-7* target
170 genes in sorted *Sftpc*-tdT^{+} and organoid transcriptome datasets. The integrated approach
171 revealed a *let-7* AT2 targetome comprised of 394 genes (Fig. 2f,g, Supplementary Data 2).
172

173 **Pathway discovery of *let-7* mRNA targetome identifies leading edge genes associated with**
174 **stem cell renewal, cell growth, and cell differentiation**

175 Functional enrichment analysis of the *let-7* targetome highlighted diverse networks of *let-*
176 *7* targets associated with an array of cellular programs including stem cell renewal, growth, and
177 differentiation (Supplementary Data 2,3). Interestingly, KEGG enrichment analysis showed the
178 top pathways as miRNAs in cancer, focal adhesion, ECM-receptor interaction, and P53 signaling
179 (Fig. 2h, Supplementary Data 3). MiRNAs typically govern cell programs upstream of transcription
180 factors (TF) and multiway hub genes in gene regulatory networks (GRN)[18-20,29]. Annotation of the
181 *let-7* targetome revealed TFs which includes gene activators (*e.g*. E2f1, *Hif1a*, *Myc*), gene
182 repressors and context dependent inducers/repressors of gene expression (*e.g*., *Bach1*, *Ezh2,*
183 *Foxp2*) (Supplementary Data 1,2,3). Major hub genes, *Kras* and *Nras* were also identified as
184 targets of *let-7* (Supplementary Data 1,2,3). ChIP-Seq regulatory analysis on transcriptome
185 datasets showed significant enrichment for MYC, E2F1, E2F6, and BACH1 targets in genes
186 upregulated after depletion of *let-7afd* (Fig. 2i, Supplementary Data 4). Targets of EZH2 were
187 overrepresented in downregulated genes upon loss of *let-7afd* (Fig. 2i). Intriguingly, the same is
188 also true for the EZH2 partner proteins SUZ12/EED and core components of the Polycomb
189 Repressive Complex 2 (PRC2) which mediate tri-methylation of histone H3 on lysine 27
190 (H3K27me3),[30,31] implying that deletion of *let-7afd* promotes EZH2 mediated epigenetic silencing

191 (Fig. 2i). Additionally, loss of *let-7afd* promotes the induction of KRAS pathway in AT2 cells
192 (Supplementary Fig. 3a). Network analysis revealed strong connectivity of hub targets implicating
193 the existence of a *let-7* dependent oncogenic GRN (OGRN) in AT2 cells (Fig. 2j). We note the
194 unique properties of OGRN genes as sufficient drivers of uncontrolled cell growth and failed
195 terminal differentiation in disease[30,32,33]. We annotated the location of the *let-7* chimeric peaks and
196 binding motifs for *let-7* within 3'UTRs (Fig. 2k,l, Supplementary Fig. 3b,c, Supplementary Data
197 1,2). *Bach1*, *E2f1*, *Ezh2*, *Myc*, *Kras*, and *Nras* contain evolutionarily conserved sites and were
198 previously identified as direct targets of *let-7* in non-AT2 cells[17-20,34]. *Hif1a* emerged as a direct
199 target of *let-7*; however, the binding site is poorly conserved in humans (Supplementary Fig. 3b,c).
200 We confirmed significant increased mRNA expression of OGRN genes by qPCR detection in
201 sorted *let-7afd*$^{+/-}$ *Sftpc-tdT*$^{+}$ cells following 14 days of iTAM (Fig. 2m, Supplementary Fig. 3d).
202

203 **Transcriptional convergence of alveolar and PSCs show enrichment of *let-7***
204 **targetome genes in ADI cells**

205 We evaluated the expression dynamics of the *let-7* targetome during AT2 cell "bridging"
206 into ADIs following bleomycin injury from a published scRNA-seq dataset[12]. At the same time, we
207 also incorporated expression data for MHC-II^{+} club cells because they were associated with
208 production of AT2 intermediate cells in bleomycin injury. Interestingly, *Bach1, Ezh2, Kras, Myc,*
209 and *Nras* expression levels were increased along the differentiation trajectory from AT2 towards
210 ADIs (Fig. 2n, Supplementary Fig. 3e). Conversion of MHC-II^{+} club cells into KRT8^{+} ADI showed
211 a more nuanced pattern for *Ezh2* and *Bach1* indicated by an increase followed by a reduction of
212 expression (Fig. 2n). Most *let-7* OGRN genes are upregulated in WT AT2 cells after 5-days of
213 bleomycin treatment, suggesting they are co-regulated during lung regeneration (Supplementary
214 Fig. 3f). Many *let-7* targets in our dataset exhibit a gradual increase and peak in expression in
215 ADIs relative to both AT2 and MHC-II^{+} club cells (Fig. 2o). The *let-7* targetome exhibits greater
216 enrichment in AT1s and transitional AT2s than hAT2s (Fig. 2p). Together, these results support

217 the notion that *let-7* serves as a braking mechanism in generation of pAT2/ADIs following lung
218 injury and alveolar regeneration upstream of a stress-inducible OGRN. These data prompted us
219 to explore the phenotypic consequences of chronic absence of *let-7afd* in pulmonary fibrosis.
220

221 **Chronic deletion of *let-7afd* in AT2 cells induces progressive and spontaneous lung**
222 **fibrosis**

223 At 1-month of iTAM (Supplementary Fig. 4a), both male and female *let-7bc2*^{AT2} and *let-*
224 *7afd*^{AT2} mice showed spatially heterogenous disruption of the distal lung architecture marked by
225 enlargement of alveolar spaces and increased presence of alveolar and peribronchial leukocytes
226 and hemosiderin-laden macrophage infiltrates (Fig. 3a,b,e, Supplementary Fig. 4b,c).
227 Approximately 30% of *let-7afd*^{AT2} mice furthermore exhibit heterogenous disorganization of alveoli
228 including septal wall thickening and the appearance of interstitial cells (Fig. 3a,b). The *let-7afd*^{AT2}
229 mice additionally show isolated areas of alveolar septal destruction, fibroblastic foci, and collagen
230 deposition primarily at the periphery of the lung (Fig. 3a,b,f,g). A parallel histologic evaluation of
231 *let-7bc2*^{AT2} mice at 1-month of iTAM indicates a milder phenotype without lung collagen deposition
232 (Fig. 3a,b,f,g). When the *let-7afd*^{AT2} mice were followed for 2-months of iTAM, they exhibit
233 resolution of pulmonary fibrosis but retain enlargement of alveolar spaces vs controls
234 (Supplementary Fig. 4d-g). Pulmonary biomechanics and spirometry measurements further
235 showed that the *let-7afd*^{AT2} mice exhibit a transient decrease in compliance and inspiratory
236 capacity after 1-month, but fully recover by 2-months of iTAM (Supplementary Fig. 4h,i).

237 To determine if continual Cre/loxP deletion of *let-7* clusters maintains pulmonary fibrosis
238 over 1-month, *let-7bc2*^{AT2} and *let-7afd*^{AT2} mice received monthly iTAM boosters for up to 6-months
239 (Supplementary Fig. 5a). With this regimen, the pulmonary inflammation, heterogeneous
240 disruption of alveolar architecture and fibrotic phenotype persisted up to 6-months in >90% of *let-*
241 *7afd*^{AT2} mice (Fig. 3c,d,f,g). In contrast, the *let-7bc2*^{AT2} mice displayed a milder ILD phenotype
242 relative to *let-7afd*^{AT2} mice but without collagen deposition (Fig. 3c,d,f,g). Pulmonary

243 biomechanics demonstrated the *let-7afd*^{AT2} mice exhibit more robust restrictive impairment in lung
244 function vs controls and *let-7bc2*^{AT2} mice (Supplementary Fig. 5b). To discern the transcriptome
245 of the *let-7afd*^{AT2} mice, we carried out bulk RNA-seq on whole lungs of mice at 6-months of booster
246 iTAM. Differential gene expression analysis and GSEA indicated significant induction of
247 inflammation and fibrosis pathways in lungs of *let-7afd*^{AT2} mice (Supplementary Fig. 5c). Overall,
248 these data establish that *let-7afd* deletion in AT2 cells models progressive spontaneous
249 pulmonary fibrosis.
250
251 **Ablation of the *let-7afd* in AT2 stimulates the persistence of ADI cells**
252 Based on this data, we hypothesized that AT2 cell loss of *let-7afd* drives the proliferative
253 expansion of fibrogenic AT2 intermediates. We validated the presence of supernumerary AT2
254 lineage cells in lungs of *let-7afd*^{AT2} mice compared to controls after 1-month of iTAM and 5-months
255 of booster iTAM respectively by IF quantification of *Sftpc*-tdT^{+} cells (Fig. 4a). Analysis of
256 contiguous lung H&E sections for fibroblastic aggregates and IF detection of KRT8 revealed the
257 spatial co-occurrence of ADIs in damaged areas with mesenchymal cell expansion and alveolar
258 destruction in *let-7afd*^{AT2} mice (Fig. 4b). Further quantitative IF analysis confirmed the persistence
259 of KRT8^{+} ADIs in lung parenchyma of *let-7afd*^{AT2} mice at 1- and 5-months of deletion (Fig. 4c,d).
260 Cells expressing KRT8 exhibited distinct cell shape including elongated squamous morphology
261 as recently described for ADIs (Fig. 4b,c)[11,12]. IF also confirmed increased *Sftpc-tdT*$^{+}$ labelled cells
262 co-expressing KRT8 or CLDN4 in *let-7afd*^{AT2} mice compared to controls (Fig. 4e,f). Reinforcing
263 our hypothesis, at 6-months of booster iTAM lungs of *let-7afd*^{AT2} mice furthermore exhibit
264 prolonged expression of ADI and ADI-7 cell markers (Fig. 4g,h).
265
266 **Deficiency of *let-7afd* AT2 cell hypertrophy and stimulates the expression of**
267 **profibrotic genes**
268 To determine whether deletion of *let-7afd* promotes AT2 cell hypertrophy and/or other

269 maladaptive ultrastructural cell changes associated with clinical ILD[5], we made use of
270 transmission electron microscopy (TEM) in lungs of mice after 3-months of booster iTAM. TEM
271 stereological analysis revealed the *let-7afd*^{AT2} mice exhibit enlarged or hypertrophic AT2 cells with
272 increased area relative to controls (Fig. 5a,b). Notably, *let-7afd*$^{-/-}$ AT2 cells also displayed
273 increased number and total cell area of lamellar bodies (LBs) with disorganized lamellae (Fig.
274 5a,b). The morphometric measurements of circularity furthermore show cell shape elongation of
275 *let-7afd*$^{-/-}$ AT2 cells compared to controls (Fig. 5a,b). Remarkably, *let-7afd*^{AT2} mice also exhibit
276 binucleated AT2 cells (11.1%, 5 of 45 cells) a unique feature not evidenced in control mice (0%,
277 0 of 44 cells) (Fig. 5a).

278 We hypothesized that *let-7* with its vast OGRN targets and impact on cell size and shape
279 might orchestrate fibrogenesis upstream of PI3K/AKT/MTOR and ECM receptor/EMT pathways.
280 Correspondingly, analysis of our RNA-seq datasets revealed that absence of *let-7afd* activates
281 these profibrotic pathways in AT2 cells (Supplementary Fig. 6a,b, Supplementary Data 3).
282 Integrative pathway annotation of the *let-7* AT2 cell targetome highlights a functionally
283 interconnected protein interactome network, consisting of over 50 gene targets of *let-7* directly or
284 indirectly involved in PI3K/AKT/MTOR and EMT pathways (Fig. 5c). Notably, this interactome
285 includes genes associated with fibrosis, such as TFs (*Myc*)[24], receptors (*Itgb3*, *Plaur*), ligands
286 (*Ctgf*, *Col5a2*), enzymes (*Nras*, *Kras*) and cytoskeletal proteins (*Tpm1*) (Fig. 5c, Supplementary
287 Fig. 6c,d,e, Supplementary Data 1,2,3). Most OGRN genes (e.g., *Bach1*, *Ezh2*) were included in
288 the network given their inductive roles in tissue fibrosis[22,23] and engagement of
289 PI3K/AKT/MTOR[33,35] and EMT[21,36] pathways respectively (Fig. 5c). To further explore the
290 potential contribution of OGRN in pulmonary fibrosis, we sought to determine whether they
291 remained significantly induced in *let-7afd*^{AT2} mice with fibrosis. Consistent with our acute
292 phenotypic analysis, transcript levels of most OGRN genes remained upregulated in sorted AT2
293 cells and lungs of *let-7afd*^{AT2} mice with fibrosis over controls (Fig. 5d,e). Furthermore, *let-7afd*^{AT2}
294 mice with fibrosis exhibit increased numbers of BACH1^{+}, EZH2^{+} or MYC^{+} *Sftpc*-tdT traced cells

295 than controls (Fig. 5f,g,h,i, Supplementary Fig. 6f,g,h). These findings suggests that absence of
296 *let-7afd* drives unchecked expression of OGRN at the top of the hierarchy and ECM structural
297 proteins downstream.
298
299 **Genetic loss of *let-7afd* makes AT2 cells vulnerable to DNA damage, senescence,**
300 **and apoptosis and impedes AT2 to AT1 terminal differentiation**
301 Studies have shown that in different models of lung injury and fibrosis, AT2 cells can
302 undergo cell senescence and/or apoptosis related to disruptions in quality control programs[5].
303 Furthermore, ADI cells are inherently prone to DNA damage and cell senescence during normal
304 injury repair and in IPF[11]. Additionally, unchecked expression of BACH1, EZH2, or MYC in non-
305 cancer cells can trigger DNA damage, senescence, and/or apoptosis [36-41]. We examined lungs of
306 mice with γH2AX as a marker of DNA damage in conjunction with the β-galactosidase activity
307 assay for cell senescence. At 1-month of deletion, lung immunostaining showed significant
308 accumulation and frequency of γH2AX$^+$ SFTPC$^+$ AT2s in *let-7afd*^{AT2} mice compared to controls
309 (Fig. 6a,b,c). Correspondingly, *let-7afd*^{AT2} mice showed robust accumulation of β-galactosidase
310 substrate X-gal in lung parenchyma, including AT2s indicating induction of a widespread cellular
311 senescence program (Fig. 6d). Then we assessed for apoptotic AT2 cells in lungs of mice by IF
312 detection of active CASP-3. This analysis revealed increased active CASP-3 *Sftpc*-tdT$^+$ labeled
313 cells in *let-7afd*^{AT2} mice relative to controls (Fig 6a,c). Congruent with these findings, sorted *Sftpc*-
314 tdT cells and whole lungs of *let-7afd*^{AT2} mice exhibit induction of DNA repair, senescence,
315 senescence-associated secretory phenotype (SASP), and apoptotic genes than controls (Fig 6f,g,
316 Supplementary Fig. 7a,b,c). Annotation of the *let-7* targetome identified *Casp3* and *Serpine1* as
317 potentially important mediators of these cell processes (Supplementary Fig. 7d,e, Supplementary
318 Data 1,2,3).
319 We posited that the persistence of ADIs in *let-7afd*^{AT2} mice might relate to impaired AT1

320 trans-differentiation. Thus, we tested whether *let-7afd* is necessary for differentiation of AT2s into
321 AT1s with lung IF with AT1 cell markers AGER and HOPX. The frequency of *Sftpc*-tdT$^+$ cells co-
322 expressing AT1 markers increased in *let-7afd*^{AT2} mice vs controls after 1-month of deletion as an
323 indication of AT1-transdifferentiation (Fig. 6a,g). However, consistent with the alveolar destruction
324 and net loss of AT1 cells, AT1 identity markers were lower in lungs of *let-7afd*^{AT2} mice than
325 controls (Supplementary Fig. 7f,g). Club epithelial cell markers were also downregulated
326 suggesting that *let-7afd* deletion also promotes damage within the airway (Supplementary Fig
327 7f,g).

328 To ascertain whether loss of *let-7afd* blunts AT2 to AT1 cell differentiation in an intrinsic
329 manner, we compared the formation of ADIs and AT1 differentiation by IF in control and *let-7afd*$^{-}$
330 $^{/-}$ AT2 cell organoids grown in AT1 cell differentiation medium (ADM) (Fig. 7a). On day 7 of ADM
331 culture, CLDN4$^+$ and KRT8$^+$ expression levels and positive cells were enhanced significantly in
332 *let-7afd*$^{-/-}$ organoids over controls which corroborates the increased ADIs in lungs of *let-7afd*^{AT2}
333 mice (Fig. 7b,c, Supplementary Fig. 8a,b). In further support of abnormal AT1 trans-differentiation,
334 *let-7afd*$^{-/-}$ organoids exhibited reduced AGER$^+$, HOPX$^+$, AQP5$^+$ cells and expression in contrast
335 with controls (Fig. 7d,e,f, Supplementary Fig. 8c,f,g). Of note, *let-7afd*$^{-/-}$ organoids also exhibit
336 reduced expression and fewer LGALS3$^+$ (a late ADI marker) cells vs controls which highlight a
337 late block in AT1 differentiation (Fig. 7d,g, Supplementary Fig. 8d). By comparison, SFTPC$^+$ cells
338 and levels were enhanced in *let-7afd*$^{-/-}$ organoids suggesting that absence of *let-7* promotes not
339 only the accumulation of ADIs but also reinforces retention of AT2 identity (Fig. 7d,h,
340 Supplementary Fig. 8e). To ascertain whether *let-7afd* depletion promotes DNA damage or death
341 in differentiation impaired *let-7afd*$^{-/-}$ organoids, we examined levels of γH2AX and active CASP3
342 by IF. The number of γH2AX$^+$ and active CASP3$^+$ cells were increased in *let-7afd*$^{-/-}$ AT2 cultures
343 compared with controls (Supplementary Fig. 8f,h,i). Thus, *let-7afd* serves as a pivotal brake to
344 the formation of lung injury inducing ADI cells, which are stalled in AT1 cell differentiation.

345 Furthermore, loss of *let-7afd* renders AT2 cells prone to senescence and apoptosis in a cell
346 intrinsic manner which could aggravate pulmonary fibrosis[42].
347 To explore potential mechanisms of impaired AT2 to AT1 trans-differentiation of *let-7afd*$^{-/-}$
348 AT2 cultures, we examined BACH1 and EZH2 expression by IF in ADM cultures. Interestingly,
349 *let-7afd*$^{-/-}$ cultured AT2 organoids exhibited higher levels and frequency of BACH1^{+} and EZH2^{+}
350 cells as compared to controls (Fig. 7d,i,j, Supplementary Fig. 8j,k). Both BACH1 and EZH2 have
351 been associated with impaired epithelial cell differentiation upon overexpression[23,43]. Analysis of
352 bleomycin-induced injury scRNA-seq dataset[12] revealed a gradual decrease in dynamic
353 expression BACH1/EZH2 and targetome as ADIs move in the direction of AT1 cell differentiation
354 (Fig. 7k, Supplementary Fig. 8l). Taken together these analyses lend support that loss of *let-7afd*
355 hampers AT2 cell "bridging" into AT1 cells, in part, via ectopic expression of BACH1/EZH2.
356
357 ***Let-7afd* orchestrates AT2 profibrotic dysfunction epigenetically via acetylation and**
358 **methylation of histone H3 on lysine 27 (H3K27)**
359 Pathologic overexpression of EZH2, BACH1, or MYC has been associated with epigenetic
360 induction and repression of genes involved in cell state transitions and cell identity at the level of
361 acetylation[44-46] and methylation[31,47] of H3K27 and other histones. We therefore hypothesized that
362 deletion of *let-7* reprograms fibrogenic AT2s by promoting the deposition of H3K27ac on
363 previously silent enhancers resulting in activation of cell growth and ADI genes, while
364 simultaneously repressing key genes via H3K27me3 deposition.
365 To test this, we conducted cleavage under targets and release using nuclease
366 (CUT&RUN)-DNA sequencing on chromatin to identify differential H3K27ac and H3K27me3
367 modifications in flow sorted *let-7afd*$^{-/-}$ compared to control *Sftpc-tdT*$^{+}$ cells on day 6 after iTAM
368 treatment (Fig. 8a, Supplementary Fig. 9a, Supplementary Data 5). In *let-7afd*$^{-/-}$ AT2 cells, we
369 observed increased H3K27ac peaks relative to control cells, which showed significant enrichment
370 of cell cycle genes (Fig. 8b, Supplementary Data 6). Conversely, increased H3K27me3 marks in

371 *let-7afd*$^{-/-}$ AT2 cells localized to development associated genes (Supplementary Fig. 9b,
372 Supplementary Data 6). To identify potential TF regulatory networks, we performed motif analysis
373 via HOMER. Several TF motifs, including BACH1, were significantly associated with H3K27ac
374 modifications (Fig. 8c, Supplementary Data 7).

375 To focus on differentially induced and repressed genes where H3K27 marks have a
376 functional impact, we integrated the CUT&RUN analyses with our bulk transcriptomic dataset
377 from sorted *let-7afd*$^{-/-}$ AT2 cells (Fig 8d, Supplementary 9c, Supplementary Data 8). This analysis
378 revealed a positive correlation between enhanced H3K27ac modifications and *let-7afd*-dependent
379 gene activation in *let-7afd*$^{-/-}$ AT2 cells (Fig. 8d). Notably, H3K27ac modifications were positively
380 correlated with the *let-7* targetome including *Bach1*, *Ezh2*, *Hif1a*, and *Myc* (Fig. 8d,e,
381 Supplementary Fig. 9d, Supplementary Data 5,8). Additionally, canonical ADI cell markers such
382 as *Cldn4* displayed increased H3K27ac modifications in *let-7afd*$^{-/-}$ AT2 cells vs controls (Fig. 8f,
383 Supplementary Fig. 9e, Supplementary Data 5,8). Interestingly, deletion of *let-7afd* also resulted
384 in combined H3K27ac and H3K27me3 co-modifications in *Sftpc* and *Bmp1* which may indicate
385 expression fine-tuning via bivalent chromatin (Fig. 8g). Of note, the antifibrotic and cell growth
386 suppressor target of EZH2, *Bambi*,[48,49] exhibits increased H3K27me3 deposition and reduced
387 expression in *let-7afd*$^{-/-}$ AT2 cells compared to controls (Fig. 8g, Supplementary Data 5,8). To
388 investigate whether the *let-7afd* deletion promotes H3K27me3, we examined subcellular
389 localization by IF in cultured AT2 organoids. H3K27me3 nuclear expression levels were
390 significantly enhanced in *let-7afd*$^{-/-}$ organoids over controls (Fig. 8h,i). In conclusion, these
391 epigenomic data highlight the integral role of *let-7afd* chromatin remodeling, where aberrant
392 enhancer H3K27ac activity and repressive H3k27me3 modifications lead to uncontrolled
393 induction of cell growth and ADI marker genes.

394

395 **Human Aberrant Basaloid (AB) cells from IPF patients exhibit enrichment of the *let-***
396 ***7* interactome.**

397 We speculated that reduced *let-7* activity in lung epithelial cells of IPF patients might
398 contribute to accumulation of AB cells. To investigate this hypothesis, we analyzed a published
399 single-cell RNA sequencing dataset from human IPF lungs[14]. Few targets of *let-7* were
400 upregulated in IPF AT2 relative to control AT2 cells (Fig. 9a,b, Supplementary Data 10). On the
401 other hand, AB cells exhibited significant enrichment of the murine *let-7* interactome relative to
402 AT1 and AT2 cells from IPF patients (Fig. 9a,b, Supplementary Data 10). Furthermore,
403 upregulated targets of *let-7* in AB cells compared to control AT2s figure prominently in fibrosis
404 pathways including ECM and EMT (Fig. 9c). Relative to AT1 and AT2 cells, AB cells furthermore
405 exhibit enrichment of EMT genes (Fig. 9d). The *let-7* OGRN genes, *ARID3A*, *BACH1*, *EZH2*,
406 *NRAS* were significantly upregulated in AB cells compared to control AT2 cells while FOXP2 and
407 MYC were repressed (Fig. 9e and Supplementary Data 10). We also evaluated for consensus
408 target signatures of EZH2 and BACH1 in IPF. This analysis found that AB cells show increased
409 EZH2 and BACH1 target signatures compared to IPF AT2 cells (Fig. 9f,g). Our analyses suggest
410 the *let-7* OGRN axis might contribute to the formation of AB cells in IPF; however further studies
411 will be required for more direct evidence.
412

413 **DISCUSSION**

414 Our study lends support to the importance of *let-7* miRNA in AT2s as a molecular
415 gatekeeper in lung homeostasis, injury, and healing. We identified transient and coordinated
416 downregulation of *let-7* family after bleomycin-induced lung injury, indicating a tightly regulated
417 post-transcriptional response which paves the way for the emergence of repair-associated AT2s.
418 This interpretation aligns with our studies indicating that AT2-cell specific genetic ablation of *let-*
419 *7afd* removes a “brake” on AT2 activation resulting in uncontrolled cell growth and accumulation
420 of ADIs in pulmonary hemorrhage which precedes a temporary chronic fibrotic remodeling phase.
421 Additionally, we discovered that *let-7* not only restricts AT2 cells from transitioning into ADI
422 intermediates but it is also crucial for exiting this state. Interestingly, with a booster Cre/loxP

423 deletion protocol, we observed that ADIs and pulmonary fibrosis were maintained in *let-7afd*^{AT2}
424 mice. We speculate that extensive cell death and senescence of *let-7afd*$^{-/-}$ AT2s may secondarily
425 recruit airway epithelial PSCs[12,50-52] which can repair the parenchyma.

426 The *let-7* miRNA family exerts broad cellular effects by silencing hundreds of target
427 mRNAs in GRNs[20]. Here we demonstrate that *let-7* simultaneously regulates an extensive GRN
428 in AT2 cells, including oncogenes such as BACH1, EZH2, and MYC previously linked to
429 uncontrolled cell growth and fibrosis[22-24,33,53]. Our data favors that this OGRN is persistently
430 upregulated in AT2 cells due to impaired *let-7* post-transcriptional regulation which would support
431 progressive pulmonary fibrosis disease. We note that the *let-7* OGRN likely functions as a
432 powerful coherent or synergistic feedforward-loop because these genes converge on similar
433 phenotypic disturbances in diseased epithelial cells. Impressively, OGRN *let-7* targets are
434 enriched in cycling and pAT2 and ADIs but their expression decreases as cells progress toward
435 AT1 identity. With permanent loss of *let-7afd*, our data indicates that AT2 cell identity is held within
436 ADI state, where the *let-7* OGRN genes are most highly expressed.

437 The leading-edge targets of *let-7*, such as EZH2, BACH1, MYC, are associated with
438 epithelial stem cell growth, transformation, and enhanced metastatic potential involving processes
439 which include EMT[30,32,36]. Moreover, published studies on *let-7* have shown that its loss stimulates
440 cell growth and EMT programs, while its overexpression limits these processes[20,21]. Intriguingly,
441 BACH1, EZH2, and MYC have also been associated with partial EMT in cancer, where epithelial
442 cells do not fully transition into mesenchymal cells but exhibit a continuum of epithelial and
443 mesenchymal traits which potentiate metastasis[54]. Lineage tracing and scRNA-seq studies
444 indicate that AT2 transitional cells do not transform into fibroblasts via EMT[10-13]; instead, they
445 adopt a mixed epithelial and mesenchymal gene expression program. Recent studies showed
446 that the accumulation of AT2 transitional cells can drive lung injury and ILD[11-13]. Given these
447 observations, we propose a model where loss of *let-7afd* contributes to partial EMT in transitional
448 AT2s via the OGRN.

449 Prior studies have highlighted the importance of BACH1, EZH2, and MYC on heritable
450 chromatin remodeling leading to phenotypic changes in cells[44-46]. Overexpression of BACH1,
451 EZH2, or MYC promote histone modifications including H3K27ac at active enhancers to facilitate
452 oncogenic cell signaling[44-46]. Furthermore, recent studies have shown that BACH1 and EZH2 can
453 promote H3K27me3 epigenetic silencing cooperatively in cells[47,55]. According to our data, the loss
454 of *let-7afd* enhances H3K27ac modifications which may lead to opening of chromatin and
455 increased accessibility of pioneer TFs to the enhancers of *let-7* targetome, thereby boosting not
456 only mRNA and protein production post-transcriptionally but also transcription output. This likely
457 amplifies the positive feedback loop with *Bach1*, *Ezh2*, *Myc* themselves acting as coherent
458 chromatin remodeling TF drivers in the establishment of a profibrotic AT2 epigenetic landscape.
459 However, the specific roles of BACH1, EZH2 and other OGRN targets as necessary and/or
460 sufficient mediators in the persistence of ADIs and pulmonary fibrosis remain largely
461 undetermined. Nonetheless, recent research on *Ezh2* has shown that its deletion hampers the
462 growth of lung epithelial cells and reduces the emergence of cycling epithelial cells and KRT8^{+}
463 transitional epithelial cells in murine organoids [56].

464 Our genetic studies to reduce *let-7* activity in AT2 cells relied primarily on phenotypic
465 studies of *let-7afd* but did not provide a mechanistic perspective on the contribution of *let-7bc2*
466 and we did not examine the role of other clusters in AT2 cells. Another limitation of our study is
467 that although we demonstrated dynamic changes in AT2 cells upon loss of *let-7afd* by integrated
468 approaches, we did not achieve transcriptomic and epigenomic depth at a single cell resolution
469 which would have allowed more insight on the role of *let-7* on AT2 cell plasticity and alveolar cell
470 niche.

471 In conclusion, our study provides insights into *let-7* as a braking mechanism to oncogene
472 dysregulation in AT2 cell-driven pulmonary fibrosis. Our observation that AB cells from IPF
473 patients express higher levels of the *let-7* targetome offers the enticing possibility that targeted
474 delivery of *let-7* could be used as a treatment. We point that several reports indicate the

475 effectiveness of targeted *let-7* delivery in mitigating fibrosis [57,58], and pharmacologic targeting of
476 EZH2 is employed against both cancer and fibrosis [59,60]. Furthermore, since AT2 cells are
477 significant source of lung adenocarcinomas and IPF patients are at high risk of cancer; we
478 propose that existing anti-cancer drugs might offer new approaches to target AB cells in patients
479 with IPF.
480

481 **MATERIALS AND METHODS**

482 **Mice and tamoxifen administration.**

483 Mice of both sexes were used for experiments. We recently described the creation and PCR
484 genotyping strategy of the C57BL/6 isogenic *let-7bc2*$^{fl/fl}$ or *let-7afd*$^{fl/fl}$ mice[26]. Mice were crossed
485 to *Sftpc*$^{tm1(cre/ERT)Blh}$ (*Sftpc-CreER*^{T2}), *Rosa26R-CAG-LSL-tdTomato (R26tdT)* purchased from JAX
486 and genotyped by PCR. For all phenotypic studies, mice aged 8-12 weeks old were given an
487 initial iTAM regimen defined as 4 doses of 160 mg/kg tamoxifen (Sigma, T5649) dissolved in corn
488 oil (Sigma, C8267) by intraperitoneal injections (i.p.) every other day. In some chronic phenotypic
489 experiments, mice received iTAM boosters following four weeks after the initial iTAM. The
490 boosters consisted of 4 doses of 80 mg/kg iTAM every other day and these were administered
491 monthly. *Let-7bc2*$^{f/f}$, *let-7afd*$^{f/f}$ or wild-type (WT) *Sftpc-tdT* mice were used as controls and treated
492 with iTAM in parallel with experimental mice. Mice were genotyped by PCR from ear clippings
493 with published primers[26]. All studies with mice were approved by the Baylor College of Medicine
494 Institutional Animal Care and Use Committee and followed the National Research Council Guide
495 for the Care and Use of Laboratory Animals.
496

497 **Physiologic measurements.**

498 Arterial oxygen saturation (SpO2) measurements were collected using the STARR Life Sciences
499 MouseOx Plus (Oakmont, Pennsylvania) on awake mice with a neck cuff sensor to obtain five
500 readings over a 30 min interval. The mice were shaved on the neck and allowed 45 minutes to

501 acclimate without restrains with a neck cuff sensor prior to good quality recordings. The lung
502 respiratory biomechanics values were obtained with the flexiVent (Scireq) system[61]. Mice
503 undergoing flexiVent procedure were subjected to anesthesia, followed by tracheostomy and
504 cannulation with an 18G metal cannula. The mice were placed under mechanical ventilation at a
505 respiratory rate of 150 breaths/min, a tidal volume of 10 mL/kg and a PEEP set at 3cmH2O in
506 enclosed chamber for pulmonary function measurements following manufacturer guidelines. The
507 average of three measurements with a coefficient of determination ≥ 0.95 were calculated for
508 each mouse.
509
510 **Lung histology and histomorphometry analysis.**
511 Mouse lungs were perfused with sterile PBS via right ventricle cardiac perfusion. For formalin-
512 fixed paraffin embedding tissues, lungs were inflated with instillation of 4% paraformaldehyde
513 (PFA) via a tracheal cannula at 25-cm H_2O pressure for 15mins and then tied by nylon suture.
514 The lungs were then transferred into 50 mL polypropylene tube containing PFA for overnight
515 fixation at 4°C. Then lung lobes were separated, transferred into tissue cassettes, and then
516 immersed in 70% ethanol at 4°C. Samples were provided to the Human Tissue Acquisition and
517 Pathology (HTAP) Core at BCM for paraffin embedding, cutting of 5μM thick sections, and staining
518 by H&E or Masson's trichrome. The PFA-fixed lung cryosections were obtained in similar manner,
519 but after the overnight fixation step in PFA at 4°C, the lungs were equilibrated with 30% sucrose
520 for 1-2 days, prior to embedding in OCT. Samples were then cut into 7-10uM thick sections for
521 the analysis. β-galactosidase (X-gal) lung staining was performed on frozen lung sections using
522 the Senescence Cells Histochemical Staining Kit (Sigma CS0030) following manufacturer
523 instructions. Hydroxyproline Colorimetric Assay Kit (Abcam, ab222941) was used to measure
524 collagen in lung lobes following kit instructions and optical density was measured using a
525 Varioskan LUX plate reader (Thermo Fisher Scientific, VL0000D0).

526

527 **Bronchoalveolar lavage and Prussian blue staining**.

528 Bronchoalveolar lavage for measurements of total and differential cell counts was done as we
529 described [26]. Prussian Blue staining of BALF cytospins was performed using the Iron Stain Kit
530 (Sigma, HT20-1KT) following kit instructions.

531

532 **Immunostaining.**

533 For immunostaining of paraffin embedded lung tissues or organoid sections, antigen retrieval was
534 performed with 1X BioCare Diva Decloaker RTU (BioCare, DV2004G1) buffer in a Decloaking
535 Chamber NxGen (BioCare, DC2012) at 95°C or 110°C for 15mins. Slides were then allowed to
536 cool in antigen retrieval buffer for 10 mins before washing in distilled water. Both paraffin
537 embedded and thawed cryo-sectioned slides were permeabilized with 0.3% Triton X-100 in 1%
538 Normal Goat Serum (Abcam, ab7481) for 10 mins. Antigen blocking was performed in 5% Normal
539 Goat Serum for 1 hour. Samples were then incubated overnight at 4°C with the following primary
540 antibodies diluted in 1% Normal Goat Serum: Rat anti-Ki67 conjugated FITC (1:50, Invitrogen,
541 11-5698-82), Mouse anti-active/pro-caspase3 (1:20, Invitrogen, MA1-91637), Mouse anti-EZH2
542 (1:100, Invitrogen, 14-9867-82), Rabbit anti-EZH2 (1:200, Cell Signaling, 5246), Rabbit anti-
543 BACH1 (1:200, Novus Biological, NBP2-55113), Mouse anti-γH2AX (1:200, Novus Biological,
544 NB100-74435), Rabbit anti-CLDN4 (1:200, Invitrogen, 36-4800), Rabbit anti-pro-SFTPC (1:200,
545 Millipore, AB3786), Rabbit anti-RFP/tdTomato (1:200, Rockland, 600-401-379), Rat anti-
546 Krt8/TROMA-I (1:20, DSHB, TROMA-I-s), Rat anti-Galectin-3/LGALS3 (1:500, Cedarlane,
547 CL8942AP), Rat anti-RAGE/AGER (1:100, R&D Systems, MAB1179-100), Rabbit anti-H3K27me
548 (1:200, Invitrogen, MA5-11198), Rabbit anti-Aqp5 (1:100, Invitrogen, PA5-36529), and Mouse
549 anti-HopX (1:200, Santa Cruz, sc-398703). The next day, samples were incubated for 1 hour at
550 room temperature in the following secondary antibodies diluted in 1% Normal Goat Serum with
551 DAPI (1:10000, Sigma, D9542): Alexa Fluor 488 goat anti-mouse (1:2000, Thermo Fisher

552 Scientific, A11029), Alexa Fluor 488 goat anti-Rabbit (1:2000, Thermo Fisher Scientific, A-32731),
553 Alexa Fluor 488 goat anti-Rat (1:2000, Thermo Fisher Scientific, A11006), Alexa Fluor 555 goat
554 anti-Mouse (1:2000, Thermo Fisher Scientific, A32727), Alexa Fluor 555 goat anti-Rabbit (1:2000,
555 Thermo Fisher Scientific, A21428), Alexa Fluor 555 goat anti-Rat (1:2000, Thermo Fisher
556 Scientific, A21434), Alexa Fluor 647 goat anti-Rabbit (1:2000, Thermo Fisher Scientific, A21244),
557 Alexa Fluor 647 goat anti-Rat (1:2000, Thermo Fisher Scientific, A21247), Alexa Fluor 790 Goat
558 anti-Rabbit (1:2000, Thermo Fisher Scientific, A11369). In some cases, paraffin embedded lung
559 sections were treated after secondary staining with TrueBlack Lipofuscin Autofluorescence
560 Quencher (Biotium, 23007) for 1 min following product instructions to block autofluorescence.
561 Slides were mounted with ProLong Glass Antifade Mountant (Thermo, P36980).
562

563 **Lung cell suspensions and purification of AT2 cells.**

564 Isolation of *Sftpc-tdT*$^{+}$ lineage derived AT2s was performed as previously described with minor
565 modifications [27,62]. Briefly, mouse lungs were perfused with cold PBS via right ventricle of the
566 heart and then inflated with 1 mL digestion solution containing 5 units/mL dispase (Corning,
567 354235), 450 units/mL collagenase type I (Gibco, 17100-017), 0.33 units/mL DNase I (Sigma,
568 10104159001), and 1X antibiotic-antimycotic (Thermo Fisher Scientific, A5955-100ML) in
569 Advanced DMEM/F-12 (Thermo Fisher Scientific, 12634028). Lung lobes were then minced into
570 1-2 mm^3 pieces, transferred into 4 mL digestion solution, and incubated at 37°C with rotation for
571 40 mins. Samples were dissociated by vigorously mixing by P1000 pipette tip until no large pieces
572 remained. Samples were filtered through a 70μm strainer, pelleted, and then resuspended in 1
573 mL RBC Lysis Buffer (Invitrogen, 00-4333-57) for 1-min before washing with 5 mL Advanced
574 DMEM/F-12 with 1X antibiotic-antimycotic. Lung cell suspensions were stained with Live/Dead
575 Fixable Blue stain (Invitrogen, L34962), Alexa Fluor 700 anti-mouse CD45.2 (Biolegend, 109822),
576 Brilliant Violet 711 anti-mouse EpCam (Biolegend, 118233), Alexa Fluor 700 anti-mouse CD31
577 (Biolegend, 102444), Brilliant Violet 421 anti-mouse Pdgfrα (Biolegend, 135923) antibodies and

578 incubated for 30 minutes in dark on ice. Cells were suspended in ice cold 1X PBS with 2% FBS
579 and filtered through a 40μm strainer followed by sorting of AT2 cells with *Sftpc-tdT* tracer on a
580 FACSAria (BD Biosciences). The purity of sorted cells was >97% and it was confirmed via
581 immunostaining with SFTPC (Supplemental Fig. 10). In initial AT2 organoid culture experiments,
582 lung cell suspensions were incubated on antibody-coated dishes at 37°C with 5% CO_2 for 45 mins
583 to remove adherent cells and immune cells as an intermediate step prior to flow sorting of AT2
584 cells as detailed above. This intermediate step was done by coating 100mm tissue culture dishes
585 with 42 μg anti-Mouse CD45 (BioLegend, 103101) and 16 μg anti-Mouse CD32 (BioLegend,
586 156402) in 7 mL PBS for 24-48 hours at 4°C as previously described.[62]
587
588 **RNA extraction and quantitative real-time PCR (qPCR).**
589 Cell pellets or lung lobes from individual mice were snap frozen in 350μl of 1:100 β-
590 mercaptoethanol in the RLT Lysis Buffer from the RNAeasy mini plus Kit (Qiagen, 74134). For
591 extraction of RNA in bulk RNA-seq lineage labelled *Sftpc*-tdT$^+$ AT2 cells (~700,000) were pooled
592 from three mice per genotype by flow sorting as indicated above. Cell samples were thawed and
593 vortexed while lung samples were homogenized for total RNA extraction intended for qPCR or
594 bulk RNA-seq. The RNAeasy mini plus Kit (Qiagen, 74134) was used for removal of genomic
595 DNA and RNA isolation. Quality control was performed with NanoDrop 2000C Spectrophotometer
596 (Thermo Fisher Scientific). Equal amount of input RNA was used for preparation of cDNA with
597 the High-Capacity cDNA Reverse Transcription Kit with RNase Inhibitor (Thermo Fisher Scientific,
598 4374966). Pre-designed Taqman probes were used with TaqMan Fast Advanced Master Mix
599 (Thermo Fisher Scientific, 4444557). *Gapdh* served to normalize gene expression by ΔΔCT
600 method. The qPCR was conducted and analyzed on ViiA 7 System (Applied Biosystems). The
601 following Taqman probes were used: *Bach1* (Mm01344527_m1), *Casp3* (Mm01195085_m1),
602 *Cdkn2a* (Mm00494449_m1), *E2f1* (Mm00432939_m1), *Ezh2* (Mm00468464_m1), *Kras*
603 (Mm00517492_m1), *Myc* (Mm00487804_m1), *Nras* (Mm03053787_s1), *Trp53*

604 (Mm01731287_m1), *Gapdh* (Mm99999915_g1). The validated and published *pri-let-7b/c2* and
605 *pri-let-7a1/d/f1* transcript Taqman probes [26] were custom designed by Applied Biosystems
606 (44411114, areptx2, arfvmhy).
607
608 **AT2 3D organoid cultures and differentiation.**
609 Culture of 3D organoids was carried out as previously described with minor modifications [27,63].
610 Lineage labeled *Sftpc*-tdT$^+$ AT2 cells were purified from 8-10 week-old mice on day 6-day after
611 iTAM treatment. AT2 cells were resuspended in thawed Cultrex UltiMatrix Matrigel (Biotechne,
612 BME001-05) at 1,000 cells/µL. For each biological replicate, organoids were initiated in each well
613 of 6-well plate into five 20 µl domes containing ~20,000 cells and incubated at 37°C with 5% CO_2
614 for 20 mins without media. When domes hardened, 2mL of alveolar maintenance media (AMM)
615 without Interleukin-1β was added to each well. The organoids were fed AMM without Interleukin-
616 1β every other day and grown for 10-14-days for subsequent analysis. For RNA-seq, the domes
617 were washed with 1 mL sterile PBS and then incubated in 1 mL Cultrex Organoid Harvesting
618 Solution (Biotechne, 3700-100-01) on ice for 1 hour. Domes were gently detached from 6-well
619 plates by spatula, resuspended in 10 mL PBS, pooled for each biological replicate, and then
620 pelleted at 300 x g for 10 mins at 4°C. Cells were washed and pelleted several times with 10 mL
621 sterile PBS to remove Matrigel. In AT2 to AT1 differentiation experiments, organoids were
622 switched from AMM into AT2-Differentiation medium (ADM) on day 10 followed by an additional
623 7-days as previously described [27,63]. For immunostaining analysis, the AT2 organoids were fixed
624 and sectioned as in previous publication[63]. Organoid colony forming efficiency (CFE) and
625 alveolosphere size diameters were quantified using FIJI (ImageJ, v2.14.0).
626
627 **Bulk RNA-seq processing, pathway enrichment, and regulatory network analysis.**
628 Purified RNA (> 800 ng) from each of the samples was used for the bulk RNA-seq analysis. RNA

629 samples with RIN scores greater than 7 were selected for RNA-seq with the Agilent Bioanalyzer
630 2100. Samples were submitted to the Genomic and RNA Profiling Core at BCM for RNA-seq and
631 library preparation. Nonstrand-specific, polyA+ -selected RNA-seq libraries were generated using
632 the Illumina TruSeq protocol. Libraries were sequenced to a median depth of 35-40 million 100-
633 bp single-end reads on a NovaSeq sequencer (Illumina). The FASTQ files underwent quality
634 control metrics (trimming), read mapping, and gene annotation (GRCm38/mm10 genome) with
635 default parameters with the RNA-seq Alignment v2.0.2 pipeline from Illumina's BaseSpace
636 (https://basespace.illumina.com/). The RNA-Seq Differential Expression v1.0.1 workflow (Illumina
637 BaseSpace) was used with default parameters to extract gene counts and to obtain differentially
638 expressed genes (DEG)s with an adjusted p value (FDR) < 0.05 between control and
639 experimental samples. Gene Ontology and pathway enrichment analysis was carried out with
640 web based tools Enrichr (https://maayanlab.cloud/Enrichr/) [64] or with Metascape
641 (https://metascape.org/) [65]. The gene set enrichment analysis was performed with GSEA v4.2.3
642 Mac application using standard settings. The epithelial cell marker gene sets used for GSEA were
643 obtained from Mouse Lung Injury & Regeneration web tool
644 (https://schillerlabshiny.shinyapps.io/Bleo_webtool/) [12] (Supplementary Data 10). The Jaccard
645 overlap scores for the *let-7* targetome were calculated by taking the size of the intersect and
646 dividing it by the size of the union from epithelial cell types defined in GSE141259 [12]. AT2 and
647 ADI pseudotime trajectory values were obtained from Strunz et al.,[12] Heatmaps and plots were
648 generated with R (v2022.12.0). To predict transcription factors whose function is impacted by *let-*
649 *7*, ChIP-Seq regulatory network analysis was performed on the *let-7afd*$^{-/-}$ RNA-seq datasets as
650 previously described [66]. Published raw data files corresponding to total RNA-seq of purified AT2
651 cells from control vs bleomycin treated mice (n = 3 mice per group) (GSE115730) [6] were extracted
652 from NCBI SRA toolkit and then processed for differential gene expression.
653
654 **Small RNA-seq data analysis.**

655 The published raw data files corresponding to small RNA-seq from lungs of mice after vehicle or
656 bleomycin treatment (GSE195773)[25] were extracted with the NCBI SRA toolkit. The SRA data
657 files were analyzed with miRNA Analysis v1.0.0 application workflow (Illumina BaseSpace). To
658 obtain mature *let-7* miRNA normalized counts, standard settings were used corresponding to
659 murine GRCm38/mm10 genome and miRbase DB v21 database. Plots were generated with R
660 (v2022.12.0) by normalizing bleomycin treated samples to untreated samples for each timepoint.
661

662 **CUT&RUN sequencing, processing, and data analysis**.

663 The CUT&RUN sequencing protocol was done as previously described [67,68]. Lineage labelled
664 *Sftpc*-tdT$^+$ AT2 cells (~100,000) were flow sorted from mice as indicated above. Cells were pooled
665 from two mice per genotype for CUT&RUN sequencing (n = 2). Cells were washed with wash
666 buffer (50 ml total H_2O with 20 mM HEPES pH 7.5, 150 mM NaCl, 0.5 mM Spermidine, and one
667 Roche Complete protein inhibitor tablet (Millipore, 11873580001). Cells were then incubated with
668 activated concanavalin-A beads (Bang Laboratories, L200731C) for fifteen minutes at room
669 temperature. Slurry was then separated with a Miltenyi MACSiMAG separator (Miltenyi 130-092-
670 168), washed once, and resuspended in wash buffer containing 0.05% digitonin (Digitonin Wash
671 buffer, Millipore, 300410). Digitonin wash buffer was used from here on out and cells kept on ice.
672 The samples were placed on chilled tube rack kept on ice when not rotating for remainder of
673 protocol. The samples were incubated with primary antibodies overnight at 4°C rotating and then
674 washed three times and incubated on rotator with Digitonin wash buffer containing pAG-MNase
675 (Epicypher 15-1016) for one hour at 4°C. Antibodies used were Rabbit anti-H3K27ac (Cell
676 Signaling Technologies, 8173; 1:50 concentration), Rabbit anti-H3K427me3 (Cell Signaling
677 Technologies, 9733; 1:50 concentration), and Rabbit anti-mouse IgG (Jackson ImmunoResearch,
678 315-005-003; 1:100). After, samples were washed three times they were resuspended in 100uL
679 Digitonin wash buffer and chilled on ice rack for two minutes. 2μL of 100mM $CaCl_2$ was added to
680 each sample to catalyze MNase cleavage. Cells were then kept at 4°C for 40 minutes. Cleavage

681 was stopped by adding equal volume stopping buffer (340 mM NaCl, 20 mM EDTA, 4 mM EGTA,
682 0.05% Digitonin, 0.05 mg/mL glycogen, 5 ug/mL RNase A, 2 pg/mL heterologous spike-in DNA
683 (Epicypher 18-1401)), and samples were heated to 37°C for 20 minutes for MNase/Histone/DNA
684 complex release into supernatant. Slurry was separated with magnetic stand, and supernatant
685 with DNA was collected into new tubes. DNA was purified with phenol chloroform extraction
686 (Thermo Fisher Scientific, 15593031) and resuspended in ultrapure water (Invitrogen, 10-977-
687 023). The samples were then submitted for library generation and sequencing to Admerahealth
688 (South Plainfield, NJ).

689 The amount of DNA was determined by Qubit 2.0 DNA HS Assay (ThermoFisher,
690 Massachusetts, USA) and quality was assessed by Tapestation High sensitivity D1000 DNA
691 Assay (Agilent Technologies, California, USA). The KAPA HyperPrep kit (Roche, Basel,
692 Switzerland) was used for library preparation. Assessment of library quality and quantity was done
693 with Qubit 2.0 DNA HS Assay (ThermoFisher, Massachusetts, USA), Tapestation High Sensitivity
694 D1000 Assay (Agilent Technologies, California, USA) for sequencing on an Illumina HiSeq 4000
695 (Illumina, California, USA) with a read length configuration of 150 paired-end (PE).

696 CUT&RUN sequencing data was trimmed for low quality reads and Illumina adapters
697 using the trim galore (0.6.10) package (https://github.com/FelixKrueger/TrimGalore). Data was
698 mapped using bowtie2 against the mouse genome UCSC build mm10. Peaks were called using
699 MACS2 with IgG serving as control in each sample. Differential peaks between control and *let-*
700 *7afd*$^{-/-}$ samples were determined using DiffReps, with a significance cutoff and FDR adjusted q
701 value < 0.05 and fold change exceeding 1.5x for H3K27ac peaks and a q value of < 0.10 with fold
702 change exceeding 1.5x for H3K27me3 peaks. Signal tracks were generated using DeepTools
703 v2.1.0 https://deeptools.readthedocs.io/en/2.1.0/index.html) and BEDTOOLS v2.31.0 suite
704 (https://bedtools.readthedocs.io/en/latest/content/bedtools-suite.html) was used for annotation of
705 differential peaks overlapping genes +/-10kb from its genebody [69]. GO terms for differential peaks
706 were determined using GREAT v4.0.4 [70]. Enriched motifs were derived using the

707 findMotifsGenome.pl HOMER tool [71]. Data peaks were visualized with the UCSC genome
708 browser.
709
710 **AGO2 eCLIP and *let-7* interactome network analysis.**
711 To obtain lung samples for AGO2-eCLIP+let-7, eight-week-old wild-type C57BL/6 mice were
712 administered with constant flow of 3.5% isoflurane during intratracheal administration of 4U/kg
713 bleomycin. The mice were then euthanized 6-days after treatment. Mouse lungs were cleared by
714 cardiac perfusion and then inflated with 1mL RNAse free PBS prior to harvesting and snap
715 freezing with liquid nitrogen. Samples were provided to EclipseBio (San Diego, California) for
716 generation of AGO2-eCLIP+let-7 libraries. The AGO-eCLIP+let-7 was performed in duplicate
717 from 2 lungs of mice with chimeric ligation of miRNA and mRNA as previously described but with
718 following modifications for lung sample processing and the enrichment of *let-7* targets [28,72]. Briefly,
719 approximately $20x10^6$ cells from the lung were plated on a dish then UV crosslinked, then pelleted
720 and suspended in 1 ml volume of eCLIP lysis mix. The lysates were then sonicated (QSonica
721 Q800R2) for 5 minutes, 30 seconds on / 30 seconds off with an energy setting of 75% amplitude,
722 followed by digestion with RNase-I (Ambion). A primary mouse monoclonal AGO2/EIF2C2
723 antibody (sc-53521, Santa Cruz Biotechnology) was pre-coupled for 1hr with Sheep Anti-Mouse
724 IgG Dynabeads (Thermo Fisher Scientific, 11202D) and then added to the homogenized lysate
725 for a 2hr immunoprecipitation (IP) at 4°C. After the IP, a 2% portion of the sample was taken as
726 paired Input and the remainder of lysate washed with eCLIP high stringency wash buffers. The
727 miRNA:mRNA chimeric ligation step was done at room temperature for 1hr with T4 RNA ligase
728 (NEB). The IP samples were then treated with alkaline phosphatase (FastAP, Thermo Fisher)
729 and then T4 PNK (NEB) for ligation of barcoded RNA adapters and isolation of AGO2-RNA
730 complexes [28,72]. To generate AGO2-eCLIP libraries enriched for *let-7* chimeras, 5' biotinylated
731 ssDNA probes antisense to murine *let-7a-5p*, *let-7b-5p*, *let-7d-5p*, *let-7f-5p* miRNAs were ordered
732 from Integrated DNA Technologies and resuspended in nuclease-free water to a final

733 concentration of 100μM. Each probe was bound individually to Capture Beads (Eclipse
734 Bioinnovations) and afterward mixed. The resulting probe-bound bead mixture was added to the
735 reserved AGO2-eCLIP enrichment fractions and allowed to hybridize over a 1.5-hour period, with
736 incrementally decreasing temperatures. Beads were washed to remove nonspecific RNAs and
737 afterward, bound RNAs were eluted from beads using a DNase treatment. Eluted RNA was
738 purified using an RNA Clean and Concentrator-5 Kit (Zymo Research, cat. #R1015/R1016) and
739 taken through reverse transcription, DNA adapter ligation, and PCR amplification to generate
740 sequencing libraries. Library sequencing was performed as SE122 on the NextSeq 2000 platform.
741 BedGraph files of *let-7* chimeric peaks were generated for visualization with UCSC genome
742 browser.

743 The AGO2-eCLIP+let-7 processing, and bioinformatics analysis was done by Eclipsebio
744 (San Diego, California) with a proprietary analysis pipeline v1 developed from several published
745 eCLIP publications [28,72]. The original bioinformatic pipelines are available
746 (https://github.com/yeolab/eclip; https://github.com/YeoLab/chim-eCLIP). A brief description
747 follows: The umi_tools (v1.1.1) tool was used to prune Unique molecular identifier (UMIs) from
748 reads. Next, cutadapt (v3.2) was used for trimming 3' adapters. Repetitive elements and rRNA
749 sequences were removed and non-repeat mapped reads mapped to murine GRCm38/mm10
750 using STAR (v2.7.7a). PCR duplicates were removed with umi_tools (v1.1.1). miRbase (v22.1)
751 miRNAs were reverse mapped to reads with bowtie (v1.2.3) and miRNA portion of each read
752 trimmed. STAR (v2.7.7a) was used to map the miRNA portion of each read to the genome. PCR
753 duplicates were trimmed, and miRNA target cluster peaks were identified with CLIPper (v2.1.0).
754 Individual clusters were annotated with corresponding miRNAs names and peaks annotated to
755 transcripts GENCODE release M25 (GRCm38.p6). Peaks present in both biological samples
756 were selected for downstream analysis. De novo HOMER (v4.11) [71] motif analysis was also
757 applied to confirm the *let-7* seed region as the most enriched motif in dataset. *Let-7* chimeric
758 peaks with overlap to the 3'UTR regions of protein coding genes were designated as the AGO2-

759 eCLIP *let-7* interactome. The Sylamer test was done as previously described[73]. Upregulated ($p <$
760 0.05) genes in *let-7afd*$^{-/-}$ *Sftpc*-tdT and/or cultured organoids were overlayed with AGO2-eCLIP
761 *let-7* interactome and experimentally validated and published *let-7* targets in miRTarbase
762 database [74] with Excel software (Microsoft). Pathway enrichment analysis for the *let-7* interactome
763 was carried out with Enrichr [64] and Metascape [65]. Protein-protein interaction networks were
764 derived from Metascape (using parameter of Combined Core) and then visualized and organized
765 with EnrichmentMap/Cytoscape (v3.10.1).
766
767 **Human IPF Atlas scRNA-seq integration.**
768 A published scRNA-seq dataset deposited in IPF Cell Atlas from control and IPF patients was
769 used[14]. The cell annotations for cell clusters were provided by the authors [14]. Cell-level expression
770 for individual genes was obtained with R package Seurat [75]. Gene signature scores were
771 generated using the UCell method. Violin plots for individual genes or gene signatures in specific
772 cell types were generated using the R statistical package v4.4.0. Dotplot expression of individual
773 gene in selected cell types were generated using Seurat [75]. The Hallmark EMT and ENCODE
774 Consensus ChIP-X gene targets for EZH2 used for UCell enrichment were obtained from Enrichr
775 [64]. BACH1 high confidence transcriptional targets were derived with the ChIP-Seq regulatory
776 network toolkit [66].
777
778 **Transmission electron microscopy (TEM) and analysis.**
779 We utilized a published protocol for fixation [6], processing and embedding of lung tissues for
780 preservation of AT2 cell lamellar body (LB) ultrastructure. Mice were euthanized, followed by an
781 incision of the IVC artery and descending aorta to allow for cardiac draining of blood. Lungs were
782 inflated with 1.2 mL of freshly prepared room temperature TEM fixative (4% paraformaldehyde,
783 2.5% glutaraldehyde, 0.02% picric acid in 0.1 M sodium cacodylate buffer, pH 7.3), tie sutured
784 and then fixed overnight at 4°C. Strips of lung tissue were dissected, washed in 0.1M sodium

785 cacodylate buffer, fixed in a solution of 1% OsO_4 and 1.5% potassium ferricyanide for 1hr with
786 gentle agitation, washed several times with 0.1M sodium cacodylate buffer and then incubated
787 overnight at 4 °C. Samples were then washed with ddH_20, stained with 1.5% uranyl acetate in the
788 dark for 1hr, dehydrated with a graded series of ethanol, infiltrated with and embedded in
789 EMbed812 epoxy resin (#14120, Electron Microscopy Sciences) and then sectioned at 100 nm
790 thickness with a Leica EM UC7 ultramicrotome. Images were collected with a JEOL JEM-
791 1400Flash TEM operating at 120 kV of accelerating voltage and equipped with a high-contrast
792 pole piece and an AMT NanoSprint15 Mk-II sCMOS camera. Images were examined with FIJI
793 (ImageJ, v2.9.0) to quantify AT2 cell area (mm2), LB area (mm2), LB number/cell area (#/mm2)
794 and AT2 cell circularity.
795
796 **Microscopy, image acquisition, and quantification.**
797 Slides were imaged on a Leica DM6000B (Leica, Wetzlar, Germany) using cameras CoolSNAP
798 HQ2 (Teledyne Photometrics, USA) or Infinity3-6UR (Teledyne Lumenera, USA). A Keyence BZ-
799 X800 microscope (Keyence, USA), an Olympus IX83 microscope (Olympus, USA), and a Nikon
800 A 1Rs confocal microscope were used for imaging. Image processing was done with BZ-X Series
801 Advanced Analysis software (Keyence) or cellSens image deconvolution software (Olympus).
802 Brightfield color images captured by Leica microscope where white balance with FIJI (ImageJ,
803 v2.14.0), and then stitched using AIVIA software (Leica, v11.0). Organoid domes were imaged on
804 6-well plates with a BioTek LionHeart LX microscope (Agilent, USA). Images were captured with
805 10X objective and stitched with built-in software. Cell counts were done manually based on
806 markers and DAPI with FIJI software. Mean Fluorescence Intensity (MFI) was measured by FIJI
807 software. Images of interest where then prepared using Adobe Photoshop and Illustrator. Mean
808 linear intercept and Ashcroft scoring measurements of mouse lung morphometry were done as
809 previously described[26,76].
810

811 **Statistical analysis.**

812 Values are represented as indicated in figure legends. P values were calculated using two-tailed
813 unpaired or paired Student's t test. Nonparametric Rank test was used for Ashcroft Scoring. 1-
814 way ANOVA with Sidak post-hoc test was used for the UCell enrichment analysis. A two-sided p
815 value < 0.05 was statistically significant. Determination of sample size for animal experiments
816 were based on pilot tests. Investigators were not blinded in the allocation of experiments. No data
817 was excluded from analysis. Mice of both genders were randomly assigned into experimental or
818 control groups for experiments. Statistical analyses were performed using GraphPad Prism
819 (v9.5.1) except for the RNA-seq and CUT&RUN which were done as described above.

820

821 **ACKNOWLEDGEMENTS**

822 We thank Drs. David Corry and Farrah Kheradmand for valuable scientific suggestions and for
823 generous sharing of lab equipment. M. Sayeeduddin for histology at the Tissue Acquisition and
824 Pathology Core (funded in part by P30 CA125123); and Joel M. Sederstrom for flow cytometry at
825 the BCM and Cell Sorting Core (funded in part from NIH (CA125123 and RR024574); we thank
826 the Texas Children's Hospital William T Shearer Center for Human Immunobiology and Dr.
827 Ronald Parchem for access to microscope equipment. Bioinformatics analysis was partially
828 supported by The Cancer Prevention Institute of Texas (CPRIT) grants RP210227 and
829 RP200504, NIEHS grants P30 ES030285 and P42 ES027725. This work was supported by grants
830 from the NHLBI (R01HL140398, HL167814 to AR; HL155672 to KYK; F31 HL164287 to BTT),
831 and NIGMS (T32 GM136554 to MS).

832

833 **AUTHOR CONTRIBUTIONS**

834 M.J.S., M.S. and A.R. conceptualized experiments, interpreted data, and wrote the manuscript.
835 M.J.S., M.S., P.A.E., B.T.T, S.L.L. carried out experiments. M.D.M. carried out the TEM imaging.
836 A.F.C. provided microscope image acquisition expertise. M.E.R-E., R.S.K. L.M.S., S.C.W., S.A.O.

performed bioinformatic data analysis. K.Y.K. provided expertise and supervision of epigenomics experiments. A.E., I.O.R., N.J.M., C.C., provided expertise and co-supervised bioinformatic data analysis.

COMPETING INTERESTS

F.R. is currently an employee at Vertex Pharmaceuticals. The remaining authors declare no competing interests.

DATA AVAILABILITY

The authors declare that all data supporting the findings of this study are available within the article and its Supplementary information files or from the corresponding author upon reasonable request. AGO2-eCLIP+let-7, bulk RNA-seq, and CUT&RUN-seq data has been deposited in the NCBI Gene Expression Omnibus database under accession code GSExxxx.

REFERENCES

1 Basil, M. C. *et al.* The Cellular and Physiological Basis for Lung Repair and Regeneration: Past, Present, and Future. *Cell Stem Cell* **26**, 482-502 (2020). https://doi.org:10.1016/j.stem.2020.03.009

2 Hogan, B. & Tata, P. R. Cellular organization and biology of the respiratory system. *Nat Cell Biol* (2019). https://doi.org:10.1038/s41556-019-0357-7

3 Basil, M. C., Alysandratos, K. D., Kotton, D. N. & Morrisey, E. E. Lung repair and regeneration: Advanced models and insights into human disease. *Cell Stem Cell* **31**, 439-454 (2024). https://doi.org:10.1016/j.stem.2024.02.009

4 Wuyts, W. A. *et al.* Idiopathic Pulmonary Fibrosis: Best Practice in Monitoring and Managing a Relentless Fibrotic Disease. *Respiration* **99**, 73-82 (2020). https://doi.org:10.1159/000504763

5 Katzen, J. & Beers, M. F. Contributions of alveolar epithelial cell quality control to pulmonary fibrosis. *J Clin Invest* **130**, 5088-5099 (2020). https://doi.org:10.1172/JCI139519

6 Chung, K. P. *et al.* Mitofusins regulate lipid metabolism to mediate the development of lung fibrosis. *Nat Commun* **10**, 3390 (2019). https://doi.org:10.1038/s41467-019-11327-1

869 7 Barkauskas, C. E. *et al.* Type 2 alveolar cells are stem cells in adult lung. *J Clin Invest*
870 **123**, 3025-3036 (2013). https://doi.org:10.1172/JCI68782
871 8 Nabhan, A. N., Brownfield, D. G., Harbury, P. B., Krasnow, M. A. & Desai, T. J. Single-
872 cell Wnt signaling niches maintain stemness of alveolar type 2 cells. *Science* **359**, 1118-
873 1123 (2018). https://doi.org:10.1126/science.aam6603
874 9 Zacharias, W. J. *et al.* Regeneration of the lung alveolus by an evolutionarily conserved
875 epithelial progenitor. *Nature* **555**, 251-255 (2018). https://doi.org:10.1038/nature25786
876 10 Choi, J. *et al.* Inflammatory Signals Induce AT2 Cell-Derived Damage-Associated
877 Transient Progenitors that Mediate Alveolar Regeneration. *Cell Stem Cell* **27**, 366-382
878 e367 (2020). https://doi.org:10.1016/j.stem.2020.06.020
879 11 Kobayashi, Y. *et al.* Persistence of a regeneration-associated, transitional alveolar
880 epithelial cell state in pulmonary fibrosis. *Nat Cell Biol* **22**, 934-946 (2020).
881 https://doi.org:10.1038/s41556-020-0542-8
882 12 Strunz, M. *et al.* Alveolar regeneration through a Krt8+ transitional stem cell state that
883 persists in human lung fibrosis. *Nat Commun* **11**, 3559 (2020).
884 https://doi.org:10.1038/s41467-020-17358-3
885 13 Wang, F. *et al.* Regulation of epithelial transitional states in murine and human
886 pulmonary fibrosis. *J Clin Invest* **133** (2023). https://doi.org:10.1172/JCI165612
887 14 Adams, T. S. *et al.* Single-cell RNA-seq reveals ectopic and aberrant lung-resident cell
888 populations in idiopathic pulmonary fibrosis. *Sci Adv* **6**, eaba1983 (2020).
889 https://doi.org:10.1126/sciadv.aba1983
890 15 Pandit, K. V. *et al.* Inhibition and role of let-7d in idiopathic pulmonary fibrosis. *Am J*
891 *Respir Crit Care Med* **182**, 220-229 (2010). https://doi.org:10.1164/rccm.200911-
892 1698OC
893 16 Kim, S. *et al.* Integrative phenotyping framework (iPF): integrative clustering of multiple
894 omics data identifies novel lung disease subphenotypes. *BMC Genomics* **16**, 924 (2015).
895 https://doi.org:10.1186/s12864-015-2170-4
896 17 Kim, H. H. *et al.* HuR recruits let-7/RISC to repress c-Myc expression. *Genes Dev* **23**,
897 1743-1748 (2009). https://doi.org:10.1101/gad.1812509
898 18 Kong, D. *et al.* Loss of let-7 up-regulates EZH2 in prostate cancer consistent with the
899 acquisition of cancer stem cell signatures that are attenuated by BR-DIM. *PLoS One* **7**,
900 e33729 (2012). https://doi.org:10.1371/journal.pone.0033729
901 19 Johnson, S. M. *et al.* RAS is regulated by the let-7 microRNA family. *Cell* **120**, 635-647
902 (2005). https://doi.org:10.1016/j.cell.2005.01.014
903 20 Ma, Y., Shen, N., Wicha, M. S. & Luo, M. The Roles of the Let-7 Family of MicroRNAs
904 in the Regulation of Cancer Stemness. *Cells* **10** (2021).
905 https://doi.org:10.3390/cells10092415
906 21 Jin, B. *et al.* Let-7 inhibits self-renewal of hepatocellular cancer stem-like cells through
907 regulating the epithelial-mesenchymal transition and the Wnt signaling pathway. *BMC*
908 *Cancer* **16**, 863 (2016). https://doi.org:10.1186/s12885-016-2904-y
909 22 Liu, Y. & Zheng, Y. Bach1 siRNA attenuates bleomycin-induced pulmonary fibrosis by
910 modulating oxidative stress in mice. *Int J Mol Med* **39**, 91-100 (2017).
911 https://doi.org:10.3892/ijmm.2016.2823
912 23 Le, H. Q. *et al.* An EZH2-dependent transcriptional complex promotes aberrant epithelial
913 remodelling after injury. *EMBO Rep* **22**, e52785 (2021).
914 https://doi.org:10.15252/embr.202152785

24 Qin, H. *et al.* C-MYC induces idiopathic pulmonary fibrosis via modulation of miR-9-5p-mediated TBPL1. *Cell Signal* **93**, 110274 (2022). https://doi.org:10.1016/j.cellsig.2022.110274

25 Strobel, B. *et al.* Time and phenotype-dependent transcriptome analysis in AAV-TGFbeta1 and Bleomycin-induced lung fibrosis models. *Sci Rep* **12**, 12190 (2022). https://doi.org:10.1038/s41598-022-16344-7

26 Erice, P. A. *et al.* Downregulation of Mirlet7 miRNA family promotes Tc17 differentiation and emphysema via de-repression of RORgammat. *Elife* **13** (2024). https://doi.org:10.7554/eLife.92879

27 Konishi, S., Tata, A. & Tata, P. R. Defined conditions for long-term expansion of murine and human alveolar epithelial stem cells in three-dimensional cultures. *STAR Protoc* **3**, 101447 (2022). https://doi.org:10.1016/j.xpro.2022.101447

28 Van Nostrand, E. L. *et al.* Robust transcriptome-wide discovery of RNA-binding protein binding sites with enhanced CLIP (eCLIP). *Nat Methods* **13**, 508-514 (2016). https://doi.org:10.1038/nmeth.3810

29 Rodriguez, A. *et al.* Requirement of bic/microRNA-155 for normal immune function. *Science* **316**, 608-611 (2007). https://doi.org:10.1126/science.1139253

30 Batool, A., Jin, C. & Liu, Y. X. Role of EZH2 in cell lineage determination and relative signaling pathways. *Front Biosci (Landmark Ed)* **24**, 947-960 (2019). https://doi.org:10.2741/4760

31 Comet, I., Riising, E. M., Leblanc, B. & Helin, K. Maintaining cell identity: PRC2-mediated regulation of transcription and cancer. *Nat Rev Cancer* **16**, 803-810 (2016). https://doi.org:10.1038/nrc.2016.83

32 Dhanasekaran, R. *et al.* The MYC oncogene - the grand orchestrator of cancer growth and immune evasion. *Nat Rev Clin Oncol* **19**, 23-36 (2022). https://doi.org:10.1038/s41571-021-00549-2

33 Zhang, X. *et al.* Bach1: Function, Regulation, and Involvement in Disease. *Oxid Med Cell Longev* **2018**, 1347969 (2018). https://doi.org:10.1155/2018/1347969

34 Hou, W., Tian, Q., Steuerwald, N. M., Schrum, L. W. & Bonkovsky, H. L. The let-7 microRNA enhances heme oxygenase-1 by suppressing Bach1 and attenuates oxidant injury in human hepatocytes. *Biochim Biophys Acta* **1819**, 1113-1122 (2012). https://doi.org:10.1016/j.bbagrm.2012.06.001

35 Yang, R. *et al.* E2F7-EZH2 axis regulates PTEN/AKT/mTOR signalling and glioblastoma progression. *Br J Cancer* **123**, 1445-1455 (2020). https://doi.org:10.1038/s41416-020-01032-y

36 Igarashi, K., Nishizawa, H., Saiki, Y. & Matsumoto, M. The transcription factor BACH1 at the crossroads of cancer biology: From epithelial-mesenchymal transition to ferroptosis. *J Biol Chem* **297**, 101032 (2021). https://doi.org:10.1016/j.jbc.2021.101032

37 Wang, X. *et al.* Bach1 Induces Endothelial Cell Apoptosis and Cell-Cycle Arrest through ROS Generation. *Oxid Med Cell Longev* **2016**, 6234043 (2016). https://doi.org:10.1155/2016/6234043

38 Zeidler, M. *et al.* The Polycomb group protein EZH2 impairs DNA repair in breast epithelial cells. *Neoplasia* **7**, 1011-1019 (2005). https://doi.org:10.1593/neo.05472

39 Zheng, W. & Yu, A. EZH2-mediated suppression of lncRNA-LET promotes cell apoptosis and inhibits the proliferation of post-burn skin fibroblasts. *Int J Mol Med* **41**, 1949-1957 (2018). https://doi.org:10.3892/ijmm.2018.3425

40 Gonzalez, M. E. *et al.* Histone methyltransferase EZH2 induces Akt-dependent genomic instability and BRCA1 inhibition in breast cancer. *Cancer Res* **71**, 2360-2370 (2011). https://doi.org:10.1158/0008-5472.CAN-10-1933

41 Kuzyk, A. & Mai, S. c-MYC-induced genomic instability. *Cold Spring Harb Perspect Med* **4**, a014373 (2014). https://doi.org:10.1101/cshperspect.a014373

42 Yao, C. *et al.* Senescence of Alveolar Type 2 Cells Drives Progressive Pulmonary Fibrosis. *Am J Respir Crit Care Med* **203**, 707-717 (2021). https://doi.org:10.1164/rccm.202004-1274OC

43 Sato, M. *et al.* BACH1 Promotes Pancreatic Cancer Metastasis by Repressing Epithelial Genes and Enhancing Epithelial-Mesenchymal Transition. *Cancer Res* **80**, 1279-1292 (2020). https://doi.org:10.1158/0008-5472.CAN-18-4099

44 Wei, Z. *et al.* MYC reshapes CTCF-mediated chromatin architecture in prostate cancer. *Nat Commun* **14**, 1787 (2023). https://doi.org:10.1038/s41467-023-37544-3

45 Kim, J. *et al.* Polycomb- and Methylation-Independent Roles of EZH2 as a Transcription Activator. *Cell Rep* **25**, 2808-2820 e2804 (2018). https://doi.org:10.1016/j.celrep.2018.11.035

46 Niu, C. *et al.* BACH1 recruits NANOG and histone H3 lysine 4 methyltransferase MLL/SET1 complexes to regulate enhancer-promoter activity and maintains pluripotency. *Nucleic Acids Res* **49**, 1972-1986 (2021). https://doi.org:10.1093/nar/gkab034

47 Wei, X. *et al.* Bach1 regulates self-renewal and impedes mesendodermal differentiation of human embryonic stem cells. *Sci Adv* **5**, eaau7887 (2019). https://doi.org:10.1126/sciadv.aau7887

48 Weber, F., Treeck, O., Mester, P. & Buechler, C. Expression and Function of BMP and Activin Membrane-Bound Inhibitor (BAMBI) in Chronic Liver Diseases and Hepatocellular Carcinoma. *Int J Mol Sci* **24** (2023). https://doi.org:10.3390/ijms24043473

49 Jiang, Y. *et al.* Histone H3K27 methyltransferase EZH2 and demethylase JMJD3 regulate hepatic stellate cells activation and liver fibrosis. *Theranostics* **11**, 361-378 (2021). https://doi.org:10.7150/thno.46360

50 Hu, Y. *et al.* Airway-derived emphysema-specific alveolar type II cells exhibit impaired regenerative potential in COPD. *Eur Respir J* **64** (2024). https://doi.org:10.1183/13993003.02071-2023

51 Lv, Z. *et al.* Alveolar regeneration by airway secretory-cell-derived p63(+) progenitors. *Cell Stem Cell* **31**, 1685-1700 e1686 (2024). https://doi.org:10.1016/j.stem.2024.08.005

52 Liu, Q. *et al.* Lung regeneration by multipotent stem cells residing at the bronchioalveolar-duct junction. *Nat Genet* **51**, 728-738 (2019). https://doi.org:10.1038/s41588-019-0346-6

53 Shen, Y. *et al.* c-Myc promotes renal fibrosis by inducing integrin alphav-mediated transforming growth factor-beta signaling. *Kidney Int* **92**, 888-899 (2017). https://doi.org:10.1016/j.kint.2017.03.006

54 Luond, F. *et al.* Distinct contributions of partial and full EMT to breast cancer malignancy. *Dev Cell* **56**, 3203-3221 e3211 (2021). https://doi.org:10.1016/j.devcel.2021.11.006

55 Yuan, Z. *et al.* Knockdown of Bach1 protects periodontal bone regeneration from inflammatory damage. *J Cell Mol Med* **27**, 3465-3477 (2023). https://doi.org:10.1111/jcmm.17916

1007 56 Byrd, A. L. *et al.* Dysregulated Polycomb Repressive Complex 2 contributes to chronic
1008 obstructive pulmonary disease by rewiring stem cell fate. *Stem Cell Reports* **18**, 289-304
1009 (2023). https://doi.org:10.1016/j.stemcr.2022.11.009
1010 57 Sun, L. *et al.* Exosomal miRNA Let-7 from Menstrual Blood-Derived Endometrial Stem
1011 Cells Alleviates Pulmonary Fibrosis through Regulating Mitochondrial DNA Damage.
1012 *Oxid Med Cell Longev* **2019**, 4506303 (2019). https://doi.org:10.1155/2019/4506303
1013 58 Huleihel, L. *et al.* Let-7d microRNA affects mesenchymal phenotypic properties of lung
1014 fibroblasts. *Am J Physiol Lung Cell Mol Physiol* **306**, L534-542 (2014).
1015 https://doi.org:10.1152/ajplung.00149.2013
1016 59 Duan, R., Du, W. & Guo, W. EZH2: a novel target for cancer treatment. *J Hematol Oncol*
1017 **13**, 104 (2020). https://doi.org:10.1186/s13045-020-00937-8
1018 60 Bao, X. *et al.* Inhibition of EZH2 prevents acute respiratory distress syndrome (ARDS)-
1019 associated pulmonary fibrosis by regulating the macrophage polarization phenotype.
1020 *Respir Res* **22**, 194 (2021). https://doi.org:10.1186/s12931-021-01785-x
1021 61 McGovern, T. K., Robichaud, A., Fereydoonzad, L., Schuessler, T. F. & Martin, J. G.
1022 Evaluation of respiratory system mechanics in mice using the forced oscillation
1023 technique. *J Vis Exp*, e50172 (2013). https://doi.org:10.3791/50172
1024 62 Chen, Q. & Liu, Y. Isolation and culture of mouse alveolar type II cells to study type II to
1025 type I cell differentiation. *STAR Protoc* **2**, 100241 (2021).
1026 https://doi.org:10.1016/j.xpro.2020.100241
1027 63 Katsura, H. *et al.* Human Lung Stem Cell-Based Alveolospheres Provide Insights into
1028 SARS-CoV-2-Mediated Interferon Responses and Pneumocyte Dysfunction. *Cell Stem*
1029 *Cell* **27**, 890-904 e898 (2020). https://doi.org:10.1016/j.stem.2020.10.005
1030 64 Kuleshov, M. V. *et al.* Enrichr: a comprehensive gene set enrichment analysis web server
1031 2016 update. *Nucleic Acids Res* **44**, W90-97 (2016). https://doi.org:10.1093/nar/gkw377
1032 65 Zhou, Y. *et al.* Metascape provides a biologist-oriented resource for the analysis of
1033 systems-level datasets. *Nat Commun* **10**, 1523 (2019). https://doi.org:10.1038/s41467-
1034 019-09234-6
1035 66 Ochsner, S. A. *et al.* The Signaling Pathways Project, an integrated 'omics
1036 knowledgebase for mammalian cellular signaling pathways. *Sci Data* **6**, 252 (2019).
1037 https://doi.org:10.1038/s41597-019-0193-4
1038 67 Skene, P. J., Henikoff, J. G. & Henikoff, S. Targeted in situ genome-wide profiling with
1039 high efficiency for low cell numbers. *Nat Protoc* **13**, 1006-1019 (2018).
1040 https://doi.org:10.1038/nprot.2018.015
1041 68 Le, D. T. *et al.* BATF2 promotes HSC myeloid differentiation by amplifying IFN
1042 response mediators during chronic infection. *iScience* **26**, 106059 (2023).
1043 https://doi.org:10.1016/j.isci.2023.106059
1044 69 Trevino, L. S. *et al.* Epigenome environment interactions accelerate epigenomic aging
1045 and unlock metabolically restricted epigenetic reprogramming in adulthood. *Nat Commun*
1046 **11**, 2316 (2020). https://doi.org:10.1038/s41467-020-15847-z
1047 70 McLean, C. Y. *et al.* GREAT improves functional interpretation of cis-regulatory
1048 regions. *Nat Biotechnol* **28**, 495-501 (2010). https://doi.org:10.1038/nbt.1630
1049 71 Heinz, S. *et al.* Simple combinations of lineage-determining transcription factors prime
1050 cis-regulatory elements required for macrophage and B cell identities. *Mol Cell* **38**, 576-
1051 589 (2010). https://doi.org:10.1016/j.molcel.2010.05.004

1052 72 Krivdova, G. *et al.* Identification of the global miR-130a targetome reveals a role for
1053 TBL1XR1 in hematopoietic stem cell self-renewal and t(8;21) AML. *Cell Rep* **38**,
1054 110481 (2022). https://doi.org:10.1016/j.celrep.2022.110481
1055 73 van Dongen, S., Abreu-Goodger, C. & Enright, A. J. Detecting microRNA binding and
1056 siRNA off-target effects from expression data. *Nat Methods* **5**, 1023-1025 (2008).
1057 https://doi.org:10.1038/nmeth.1267
1058 74 Huang, H. Y. *et al.* miRTarBase update 2022: an informative resource for experimentally
1059 validated miRNA-target interactions. *Nucleic Acids Res* **50**, D222-D230 (2022).
1060 https://doi.org:10.1093/nar/gkab1079
1061 75 Satija, R., Farrell, J. A., Gennert, D., Schier, A. F. & Regev, A. Spatial reconstruction of
1062 single-cell gene expression data. *Nat Biotechnol* **33**, 495-502 (2015).
1063 https://doi.org:10.1038/nbt.3192
1064 76 Hubner, R. H. *et al.* Standardized quantification of pulmonary fibrosis in histological
1065 samples. *Biotechniques* **44**, 507-511, 514-507 (2008). https://doi.org:10.2144/000112729
1066

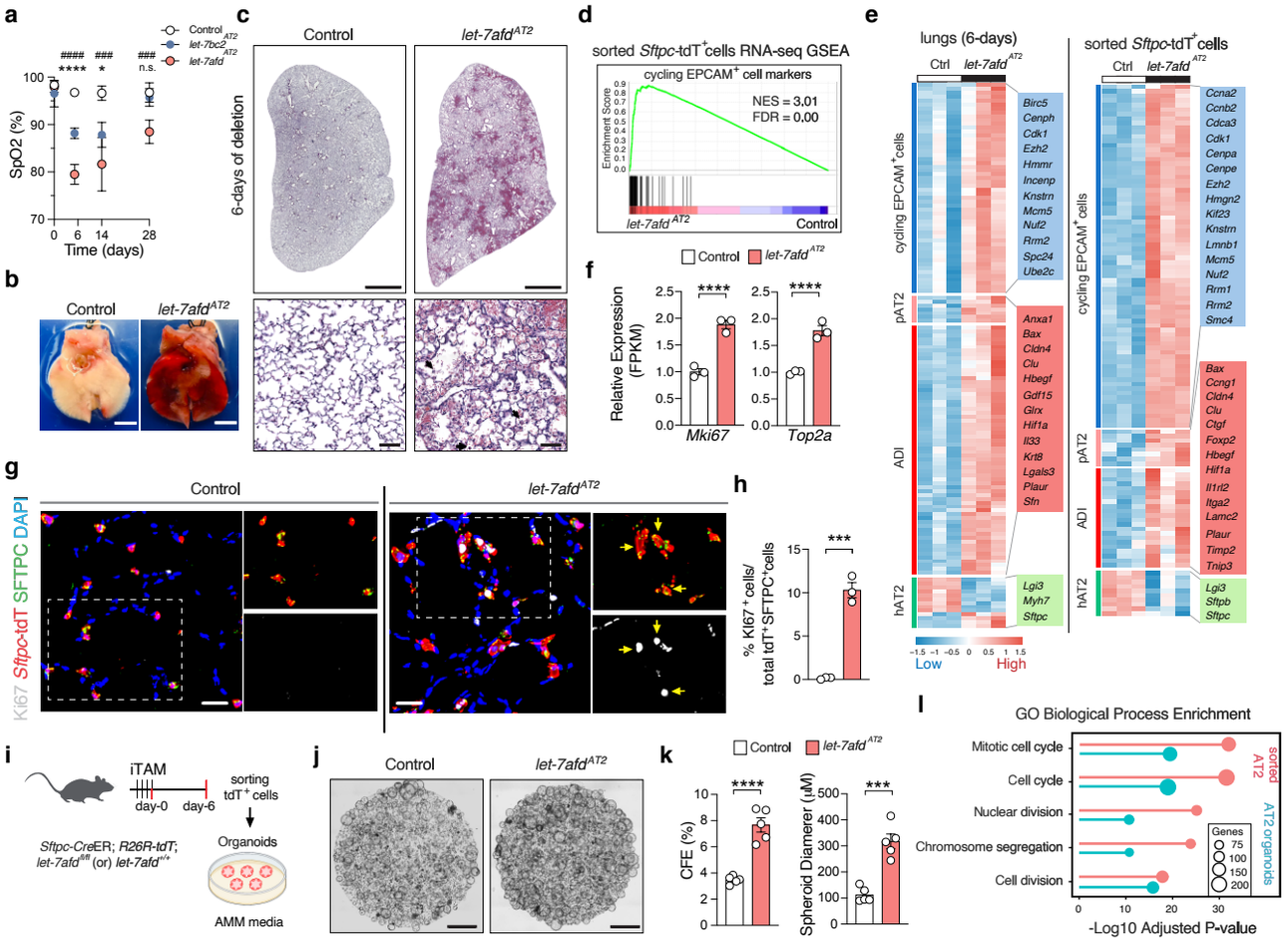

Fig. 1 Deletion of *let-7afd* in AT2 cells promotes spontaneous lung injury and AT2 transitional cells acutely. **a** Quantitative measurements of Sp02 from control, *let-7bc2*^{AT2}, *let-7afd*^{AT2} mice (n = 5 per group) following iTAM. Data are mean±s.d. **let-7bc2*^{AT2} vs control, $^{\#}$*let-7afd*^{AT2} vs control; **, $p < 0.01$, $^{\#\#\#}$, $p < 0.001$, **** and $^{\#\#\#\#}$, $p < 0.0001$ by one way ANOVA with Tukey's correction. Not significant (NS). **b-c** Representative lung dissections (**b**) and H&E-stained lung sections (**c**) from indicated mice 6-days after iTAM. Scale bars: 5 mm (**b**); 2 mm upper panel; 50 μm lower panel (**c**). Arrowheads indicate leukocytes. **d** GSEA plot shows induction of cycling epithelial genes in *let-7afd*$^{-/-}$ *Sftpc*-tdT^{+} sorted AT2 cells (n = 3 samples per group). **e** Heatmap shows differentially expressed AT2 transition markers obtained by RNA-seq from whole lung or sorted *Sftpc*-tdT^{+} AT2 cells upon deletion of *let-7afd* vs controls after 6 days of iTAM. Adjusted p value < 0.05 vs control. **f** Transcript expression by RNA-seq in *Sftpc*-tdT^{+} AT2 cells after 6 days of iTAM (n = 3 samples per group). Data are mean±s.e.m. ****adjusted $p < 0.0001$. **g,h** Representative immunostaining (**g**) and quantification (**h**) of KI67^{+}*SFTPC*$^{+}$*Sftpc*-tdT^{+} cells in lungs of *let-7afd*^{AT2} mice vs control mice 14-days after iTAM. KI67 (gray), SFTPC (green), *Sftpc*-tdT (red), DAPI (blue). (n = 3 mice per group). Data are mean±s.e.m. ***$p < 0.001$ by unpaired Student's t test. Arrows indicate KI67^{+}*SFTPC*$^{+}$*Sftpc*-tdT^{+} cells (scale bar 25 μm). **i** Schematic representation to establish AT2 organoid cultures in mice. **j** Brightfield images show *let-7afd*$^{-/-}$ vs control AT2 organoids cultured in AMM. Scale bars 1 mm. **k** Quantification of CFE and spheroid diameters of organoids in panel (**j**). Data are mean±s.e.m (n = 5 mice per group). ***$p < 0.001$, ****$p < 0.0001$ by unpaired Student's t test. Each dot represents one mouse. **l** GO BP enrichment analysis for overrepresented terms upon deletion of *let-7afd* in *Sftpc*-tdT^{+} AT2 cells (n= 3 samples per group) or organoid cultures (n = 2 mice per group) by RNA-seq. Scale shows adjusted p values. **a-c, g-h**, **j**, **k** Are representative of three independent experiments.

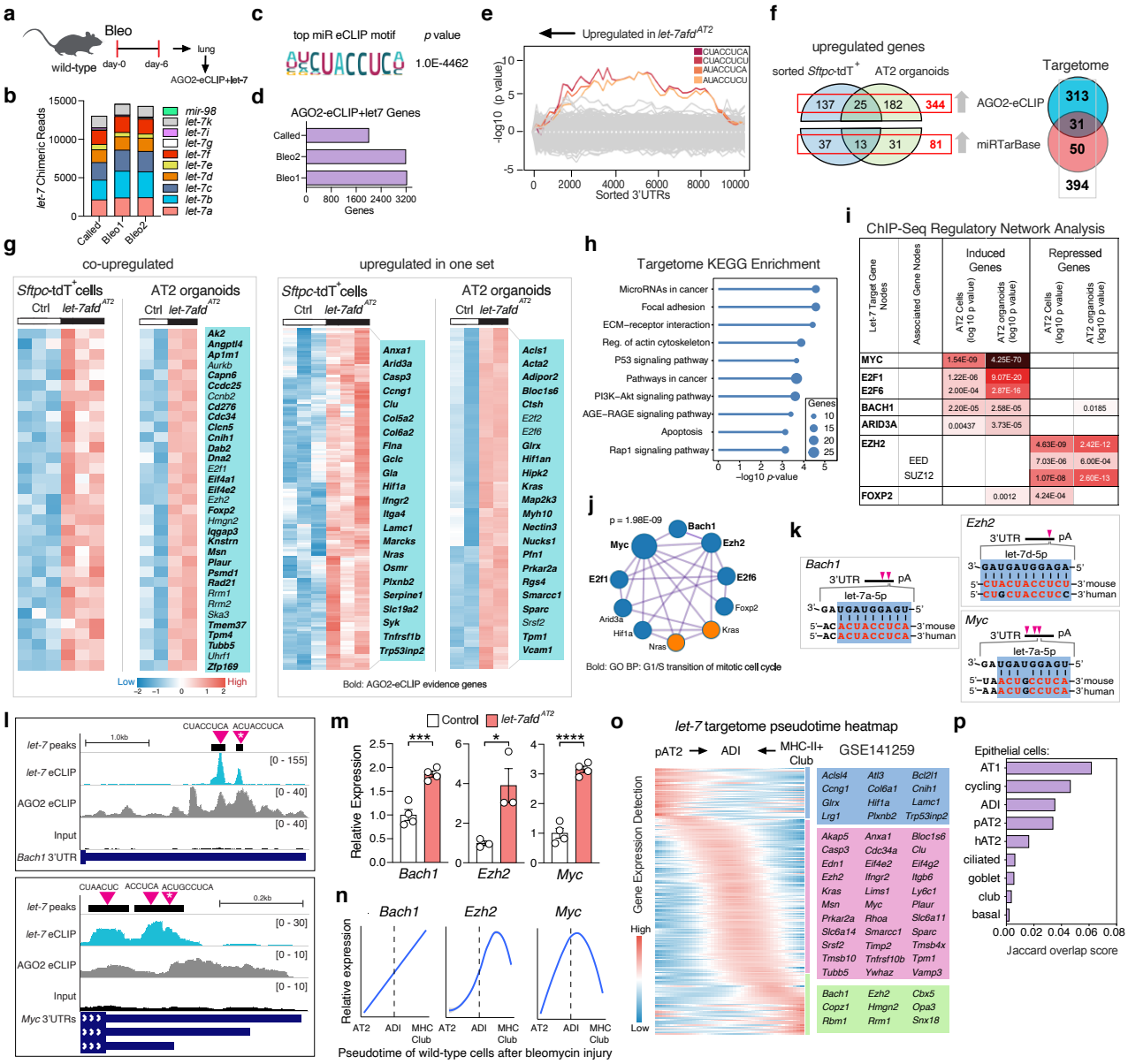

Fig. 2 Chimeric AGO2 eCLIP and transcriptomics identify *let-7* targetome in AT2 cells. **a** Schematic of experimental design for AGO2-eCLIP+let-7 analysis from lungs of mice after bleomycin treatment. **b** Fractional representation of *let-7*:mRNA chimeric reads of *let-7* members. **c** The *let-7* family binding motif is highly enriched. **d** Total number of genes with *let-7*:mRNA chimeric peaks. **e** Sylamer analysis shows overrepresentation of *let-7* binding motifs in *let-7afd*$^{-/-}$ *Sftpc*-tdT^{+} cells. **f** Venn Diagram shows gene totals to obtain the *let-7* AT2 cell targetome. **g** Heatmaps shows relative expression of significantly upregulated and validated *let-7* target genes upon loss of *let-7afd* in *Sftpc*-tdT^{+} AT2 cells (n= 3 samples per group) or AT2 organoids (n = 2 mice per group) bulk RNA-seq datasets. Adjusted p value < 0.05 vs controls. **h** KEGG pathway enrichment analysis for the *let-7* targetome. **i** ChIP-Seq cistromic analysis indicate significant enrichment of nodes corresponding to the transcription factor (TF) targets of *let-7* in sorted *let-7afd*$^{-/-}$ *Sftpc*-tdT^{+} cells and organoids. **j** Functional pathway and protein interactome network shows significant connectivity of *let-7* hub targets. TFs (blue), enzymes (orange). Cytoscape/Enrichment Map P value. **k** Schematic alignments of *let-7* "seed" region with target mRNA sequences in mice and humans. **l** UCSC genome browser tracks from AGO2-eCLIP+let-7 indicates binding of *let-7* family to the 3'UTR of genes. Purple triangles indicate motifs of *let-7*. White asterisks indicate sequence alignment in panel (**k**). **m** qPCR analysis of indicated *let-7* targets from *let-7afd*$^{-/-}$ vs control sorted *Sftpc*-tdT^{+} cells 14-days after iTAM. (n = 3-4 per group). Data are mean±s.e.m. ****p < 0.0001, ***p < 0.001, *p < 0.05 by unpaired Student's t test. **n** Line plots show smoothed relative expression levels of hub genes across the ADI pseudotime trajectories after bleomycin injury (GSE141259). Dashed line corresponds to *Krt8* peak and gray colors represent the 95% confidence interval derived from smoothing fit. **o** The expression pattern for 217 of 394 *let-7* targetome genes along the AT2 or MHC-II^{+} club cell trajectory into ADIs is based on inferred likelihood of detection. **p** Jaccard overlap scores were calculated between *let-7* targetome and epithelial cell types defined in GSE141259.

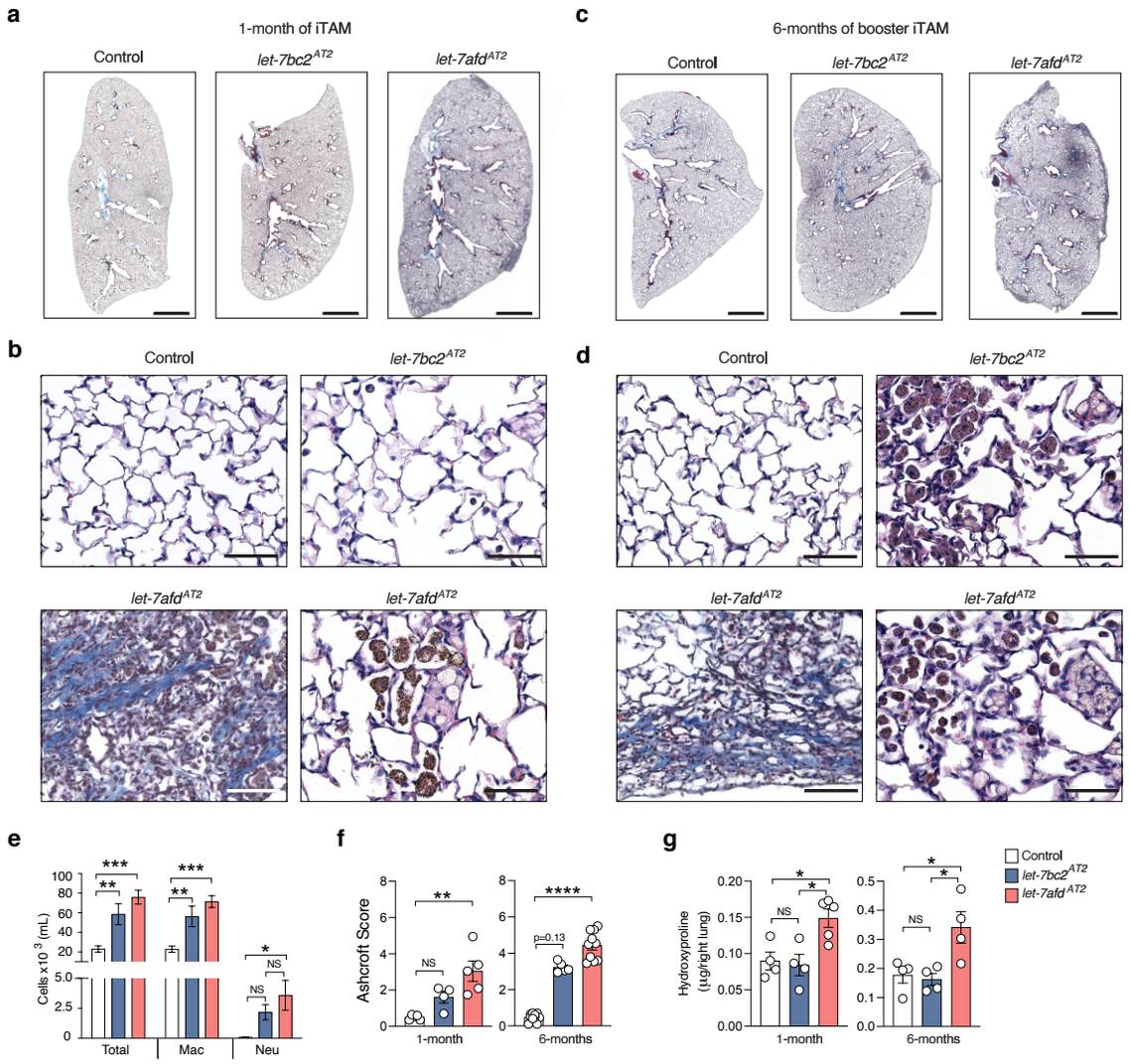

Fig. 3 AT2-specific deletion of *let-7* clusters induce spontaneous progressive chronic inflammation and ILD. **a**-**d** Representative Masson's trichrome-stained sections of lung lobes at 1-month iTAM (**a**,**b**) or 6-months (**c**,**d**) booster-iTAM. Scale bars: 2 mm upper panels; 50 μm lower panels (n = 16 mice per group). **e** Differential cell counts from BALF of mice is shown. Data are mean±s.e.m from individual mice (n = 7-8 mice per group). ***p < 0.001, **p < 0.01, *p < 0.05, by one way ANOVA with Tukey's correction. Macrophages (Mac), Neutrophils (Neu). **f** Ashcroft score was used to evaluate lung injury after iTAM. (1-month, n = 4-5 per group; 6-months, n = 5 *let-7bc2*^{AT2}, n = 10 controls and *let-7afd*^{AT2}). Data are mean±s.e.m. ****p < 0.0001, **p < 0.01, by Dunn's multiple comparison test. **g** Hydroxyproline levels from lungs of control, *let-7bc2*^{AT2}, *let-7afd*^{AT2} mice at 1-month iTAM (n = 4-5 mice per group) or 6-months of booster iTAM (4 mice per group). Data are mean±s.e.m.*p < 0.05 by one way ANOVA with Tukey's correction. **f**,**g** Each circle represents a mouse. **a**-**g** Representative of three independent experiments. Not significant (NS).

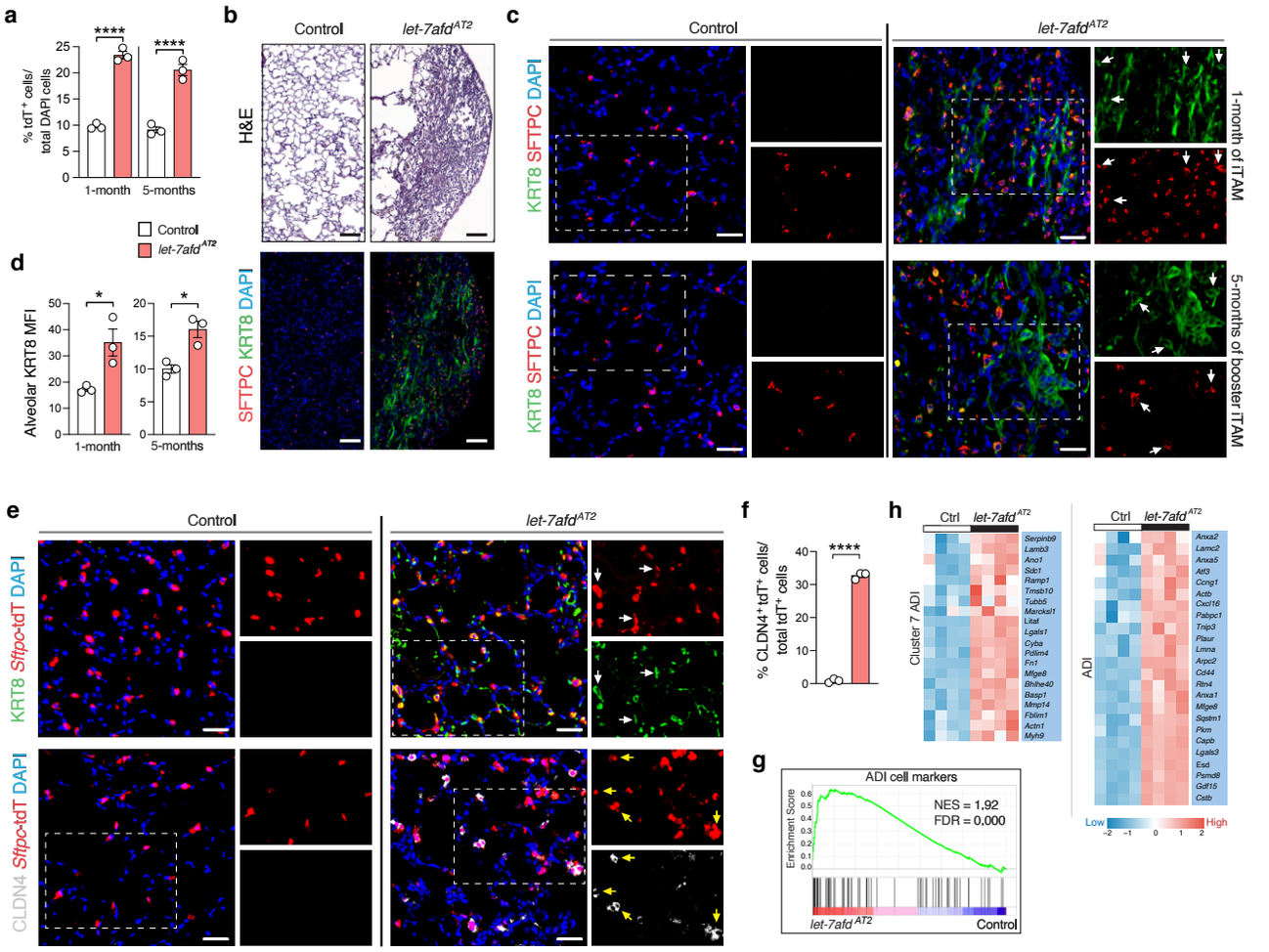

Fig 4 Ablation of *let-7afd* in AT2 cells stimulates the persistence of lung ADI intermediate cells. **a** Quantification of *Sftpc*-tdT$^+$ cells from total DAPI cells in alveolar regions of *let-7afd*^{AT2} mice compared to control mice at 1- or 5-months of booster iTAM (n = 3 mice per group). Data are mean±s.e.m. ****p < 0.0001 by unpaired Student's t test. **b** Representative H&E-stained (upper panels) and immunostaining (lower panels) serial sections of lung after 1 month of iTAM in *let-7afd*^{AT2} mice compared to control mice. IF shows KRT8 (green), SFTPC (red), DAPI (blue). Scale bars: 50 μm. **c** Representative immunostaining of KRT8 (green), SFTPC (red), DAPI (blue) at 1 month (upper panels) or 5 months of booster iTAM (lower panels) in *let-7afd*^{AT2} mice vs controls. Arrowheads point to KRT8$^+$SFTPC$^+$ cells. Scale bars: 25μm. **d** Quantification of KRT8 mean fluorescence intensity (MFI) from alveolar regions excluding airways of mice groups in panel (**c**) (n = 3 mice per group). Data are mean±s.e.m. *p < 0.05 by unpaired Student's t test. **e** Representative immunostaining of *Sftpc*-TdT$^+$ traced KRT8$^+$ or CLDN4$^+$ cells in lungs of *let-7afd*^{AT2} mice compared to controls 1-month post-iTAM. KRT8 (green), CLDN4 (gray), *Sftpc*-tdT (red), DAPI (blue). Arrowheads point to KRT8$^+$ or CLDN4$^+$ *Sftpc*-tdT$^+$ cells. Scale bars: 25 μm. **f** Quantification of *Sftpc*-tdT$^+$CLDN4$^+$ from total *Sftpc*-TdT$^+$ cells at 1-month post-iTAM (n = 3 mice per group). Data are mean±s.e.m. ****p < 0.0001, by unpaired Student's t test. **g,h** GSEA and heat map plots derived from RNA-seq show significant induction of ADI genes in lungs of *let-7afd*^{AT2} mice vs controls with 6-months of booster iTAM (n = 4 per group). Adjusted p value < 0.05 vs controls. **a-f** Representative of three independent experiments.

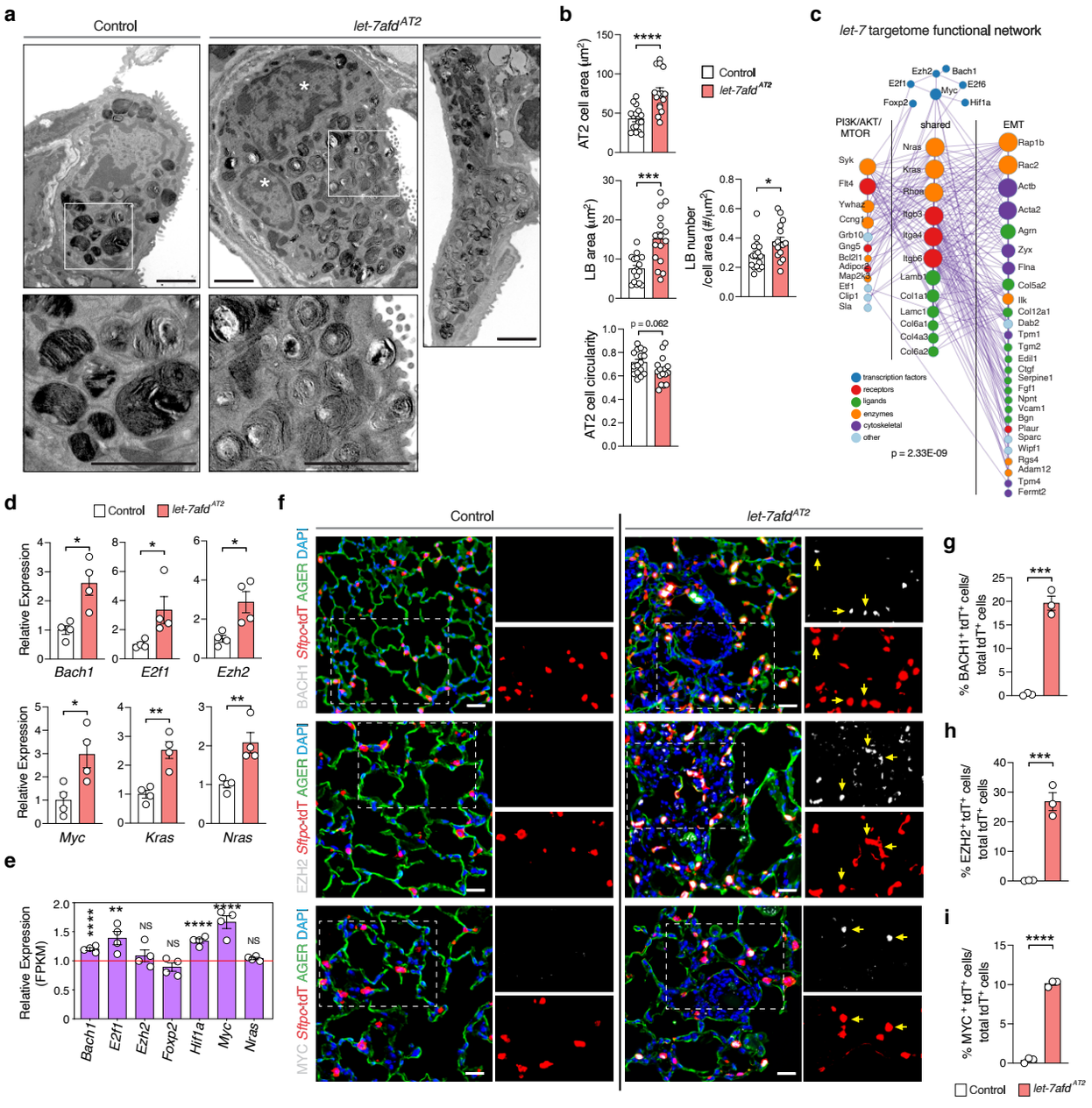

Fig 5 Loss of *let-7afd* stimulates AT2 cell hypertrophy and induces the expression of *let-7* target genes associated with cell hypertophy, ECM remodeling, and fibrosis. **a** Representative TEM image shows an enlarged *let-7afd*$^{-/-}$ AT2 cell with increased abnormal lamellar bodies (LB)s and more than one nuclei (n = 3 mice per group). The white asterisks point to individual nuclei. An elongated *let-7afd*$^{-/-}$ AT2 cell is shown on right. Scale bars: 2 μm. **b** TEM quantification of cell area and LB cell area (μm^2), LB number per μm^2 of cell area, and cell circularity index in each AT2 cell. Data are mean±s.e.m. Each dot represents one AT2 cell (control AT2 cells n = 16; *let-7afd*$^{-/-}$AT2 cells = 16, from a total of 3 mice per group; ****$p < 0.0001$, ***$p < 0.001$, *$p < 0.05$, and $p = 0.062$ by unpaired Student's t test. **c** Functional network of *let-7* target genes associated with PI3K/AKT/MTOR and/or EMT. Network p value was computed by Cytoscape/ Enrichment Map. **d** Expression levels of hub *let-7* targets were evaluated by qPCR after 2 months booster-iTAM from *let-7afd*$^{-/-}$ and control *Sftpc*-tdT$^+$ cells (n = 4 samples per group; from pools of 2 mice). Data are mean±s.e.m. **$p < 0.01$, *$p < 0.05$, by unpaired Student's t test. **e** *Let-7* target expression was determined by RNA-seq in lungs of *let-7afd*^{AT2} and control mice after 6-months of booster iTAM (n = 4 samples per group). Data are mean±s.e.m plotted relative to control samples = 1.0. **adjusted $p < 0.01$, ****adjusted $p < 0.0001$. Not significant (NS). **f** Representative IF images show increased numbers of BACH1$^+$ (top panels), EZH2$^+$ (middle panels), and MYC$^+$ *Sftpc*-tdT$^+$ cells respectively (indicated by yellow arrows) in lungs of *let-7afd*^{AT2} mice vs control mice lungs after 1-month of iTAM. BACH1 (gray); EZH2 (gray); MYC (gray), *Sftpc*-tdT (red); AGER (green); DAPI (blue). Scale bars: 25 μm. **g-i** Quantification of BACH1$^+$ (**g**), EZH2$^+$ (**h**), and MYC$^+$ (**i**) *Sftpc*-tdT$^+$ cells in total *Sftpc*-tdT$^+$ cells (n = 3 mice per group). Data are mean ±s.e.m. ****$p < 0.0001$, ***$p < 0.001$ by unpaired Student's t test. **f-i** Representative of three independent experiments.

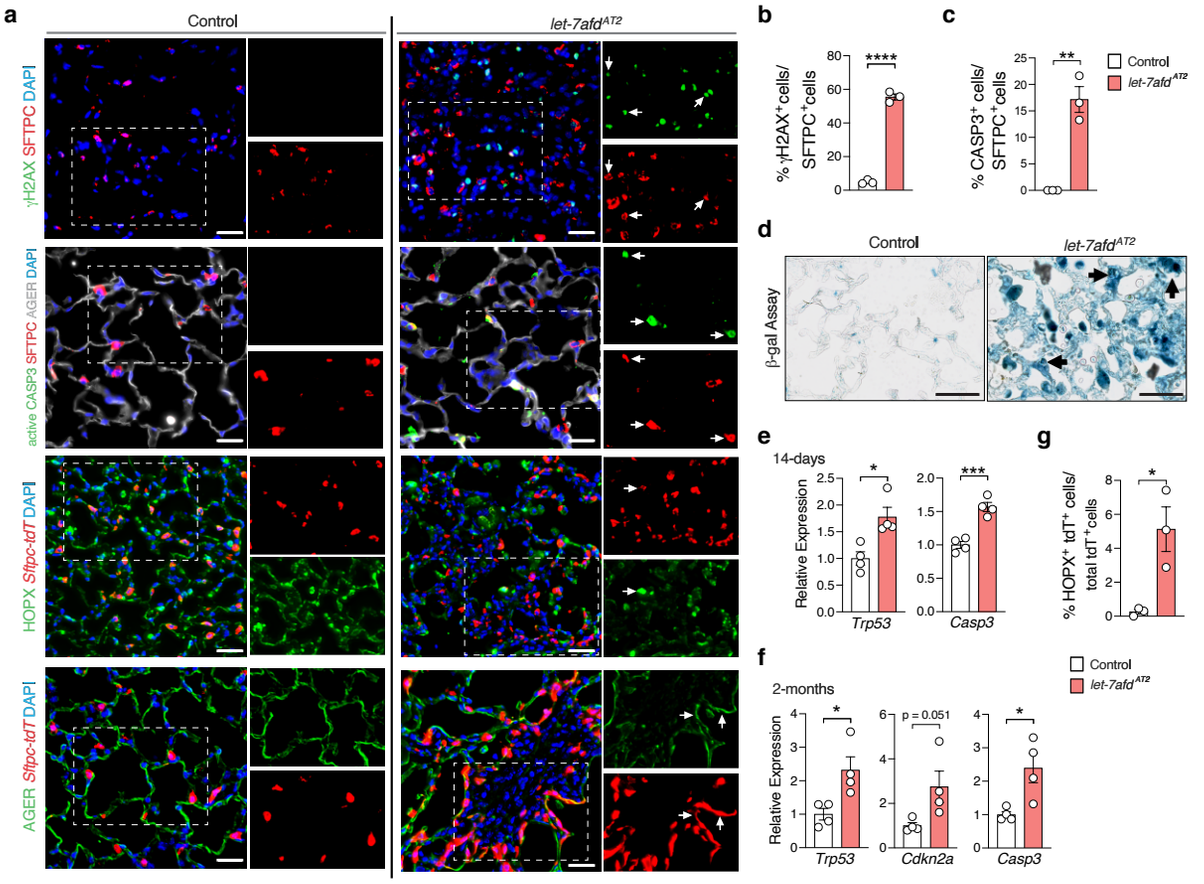

Fig 6 Loss of *let-7afd* is associated with AT2 cell DNA damage, senescence, and apoptosis. **a** Immunostaining for γH2AX (green), SFTPC (red), DAPI (blue) upper panels; active CASP3 (green), SFTPC (red), AGER (gray), DAPI (blue) second row panels; HOPX (green), *Sftpc*-tdT (red), DAPI (blue) third row panels; AGER (green), *Sftpc*-tdT (red), DAPI (blue) lower panels in lungs of *let-7afd*^{AT2} and control mice after 1 month of iTAM. Arrows indicate γH2AX$^+$SFTPC$^+$ cells, active-CASP3$^+$SFTPC$^+$ cells, HOPX$^+$*Sftpc*-tdT$^+$, and AGER$^+$*Sftpc*-tdT$^+$cells respectively. Scale bars: 25 μm. **b-c** Quantification of γH2AX$^+$SFTPC$^+$ cells (**b**) or active-CASP3$^+$ SFTPC$^+$ cells (**c**) from total SFTPC$^+$ cells (n = 3 mice per group). Data are mean±s.e.m. ****$p < 0.0001$, **$p < 0.01$, by unpaired Student's t test. **d** Representative β-galactosidase staining in lungs of *let-7afd*^{AT2} and control mice after 1-month of iTAM. Arrowheads point to AT2 cells in thickened alveolar septa (n = 6 mice per group). Scale bars: 50 μm. **e,f** Indicated genes were detected by qPCR from *let-7afd*$^{-/-}$ and control *Sftpc*-tdT$^+$ cells after 14-days of iTAM (**e**) or 2-months (**f**) of booster iTAM (n = 4 samples per group from pools of 2 mice). Data are mean±s.e.m. *$p < 0.05$, ***$p < 0.001$, by unpaired Student's t test. **g** Quantification of HOPX$^+$*Sftpc*-tdT$^+$ cells from total *Sftpc*-TdT$^+$ cells in lungs of *let-7afd*^{AT2} and control mice at 1-month after iTAM (n = 3 mice per group). Data are mean±s.e.m. *$p < 0.05$, by unpaired Student's t test. **a-g** Representative of three independent experiments.

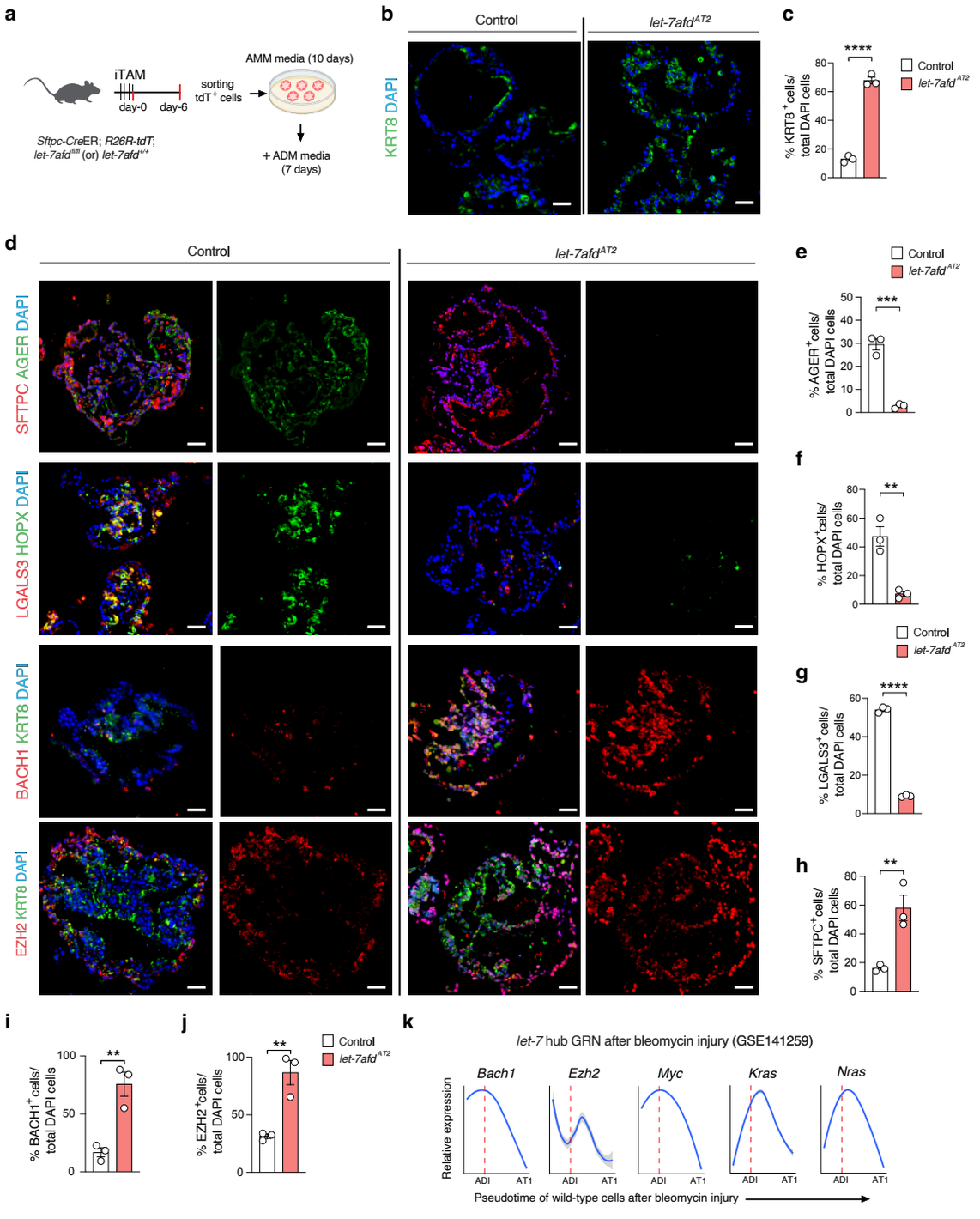

Fig 7 Absence of *let-7afd* impairs AT2 to AT1 differentiation. **a** Schematic representation of experimental design to examine the role of *let-7afd* in AT2 to AT1 differentiation in cultured AT2 organoids. **b**,**d** Representative immunostaining of ADI, AT1 markers and BACH1/EZH2 expression in *let-7afd*$^{-/-}$ vs control AT2 organoids grown as in panel (**a**) (n = 3 mice per group). Panel (**b**) shows KRT8 (green), DAPI (blue). Panel (**d**) shows AGER (green), SFTPC (red), DAPI (blue) top row panels; HOPX (green); LGALS3 (red); DAPI (blue) second row panels; BACH1 (red), KRT8 (green), DAPI (blue) third row panels; EZH2 (red), KRT8 (green), DAPI (blue) bottom row panels. Scale bars: 25 μm. **c**,**e-j** Quantification of KRT8$^+$ (**c**), AGER$^+$ (**e**), HOPX$^+$ (**f**), LGALS$^+$ (**g**), SFTPC$^+$ (**h**), BACH1$^+$ (**i**), or EZH2$^+$ (**j**) cells respectively in total DAPI cells (n = 3 mice per group). Data are mean±s.e.m. ****$p < 0.0001$, ***$p < 0.001$, **$p < 0.01$, by unpaired Student's t test. Each circle represents a mouse. Representative of three independent experiments. **k** Line plots show smoothed expression levels of selected *let-7* hub targets in the ADI to AT1 trajectory obtained from GSE141259 dataset. Grey line represents 95% confidence interval obtained from fit model. KRT8 peak represented by dashed line.

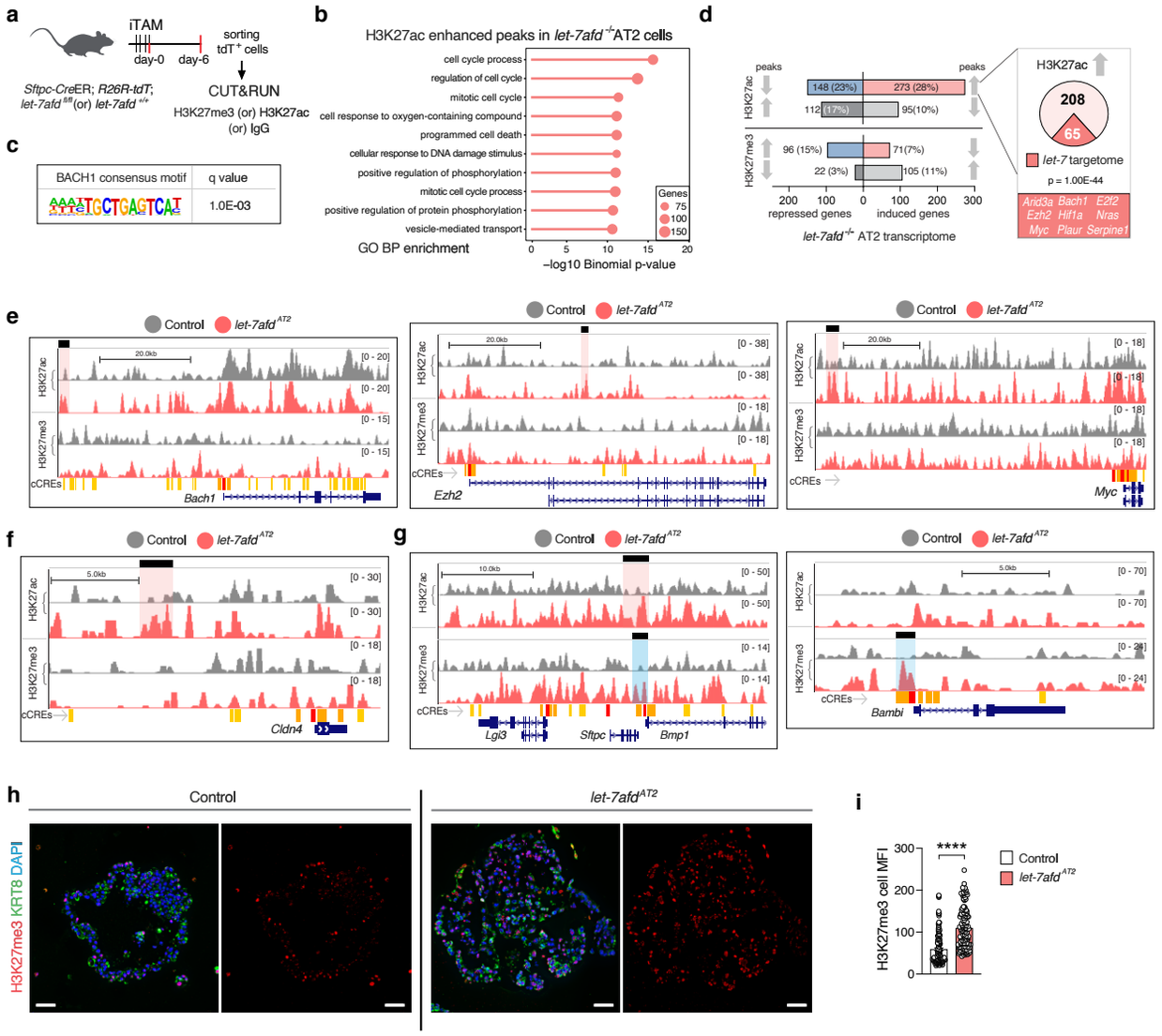

Fig 8 Loss of *Let-7afd* orchestrates AT2 fibrotic reprogramming, in part, epigenetically via H3K27 acetylation and methylation. **a** Experimental design scheme to carry out CUT&RUN from sorted *Sftpc*-tdT$^+$ cells obtained from *let-7afd^{AT2}* mice or control mice (n = 2 mice per group). **b,c** GO biological pathway (BP) (**b**) and HOMER transcription factor motif (**c**) enrichment of induced H3K27ac peaks in *let-7afd$^{-/-}$* compared to control *Sftpc*-tdT$^+$ cells. **d** Integration analysis of CUT&RUN with RNA-seq in *let-7afd$^{-/-}$* vs control *Sftpc*-tdT$^+$ cells shows correlation with transcription. Gene totals of congruent-expression change directionality (blue+red) and incongruent directionality (gray) are shown for H3K27ac and H3K27me3. Pie chart and ORA gene enrichment analysis shows that a high fraction of upregulated *let-7* targetome genes exhibit H3K27ac marks suggestive of increased enhancer activity in *let-7afd$^{-/-}$ Sftpc*-tdT$^+$ cells. **e-g** UCSC tracks show H3K27ac and H3K27me3 peaks in selected genes in *let-7afd$^{-/-}$ Sftpc*-tdT$^+$ cells compared to controls. Enriched H3K27ac peaks in *let-7afd$^{-/-}$ Sftpc*-tdT$^+$ cells are shaded in red. The enriched H3K27me peaks in *let-7afd$^{-/-}$ Sftpc*-tdT$^+$ cells vs controls are highlighted in blue. ENCODE candidate cis-regulatory elements (cCREs). **h** Representative immunostaining of H3K27me3$^+$ cells in *let-7afd$^{-/-}$* vs control AT2 organoids in ADM (n = 3 per group). H3K27me3 (red), KRT8 (green), DAPI (blue). Scale bars: 25 μm. **i** Quantification of H3K27me3$^+$ nuclear MFI expression. Data are mean±s.e.m. Each dot represents one cell (n = 149 cells per genotype, 3 mice per group). Data are mean±s.e.m. ****$p < 0.0001$, by unpaired Student's t test. Representative of three independent experiments.

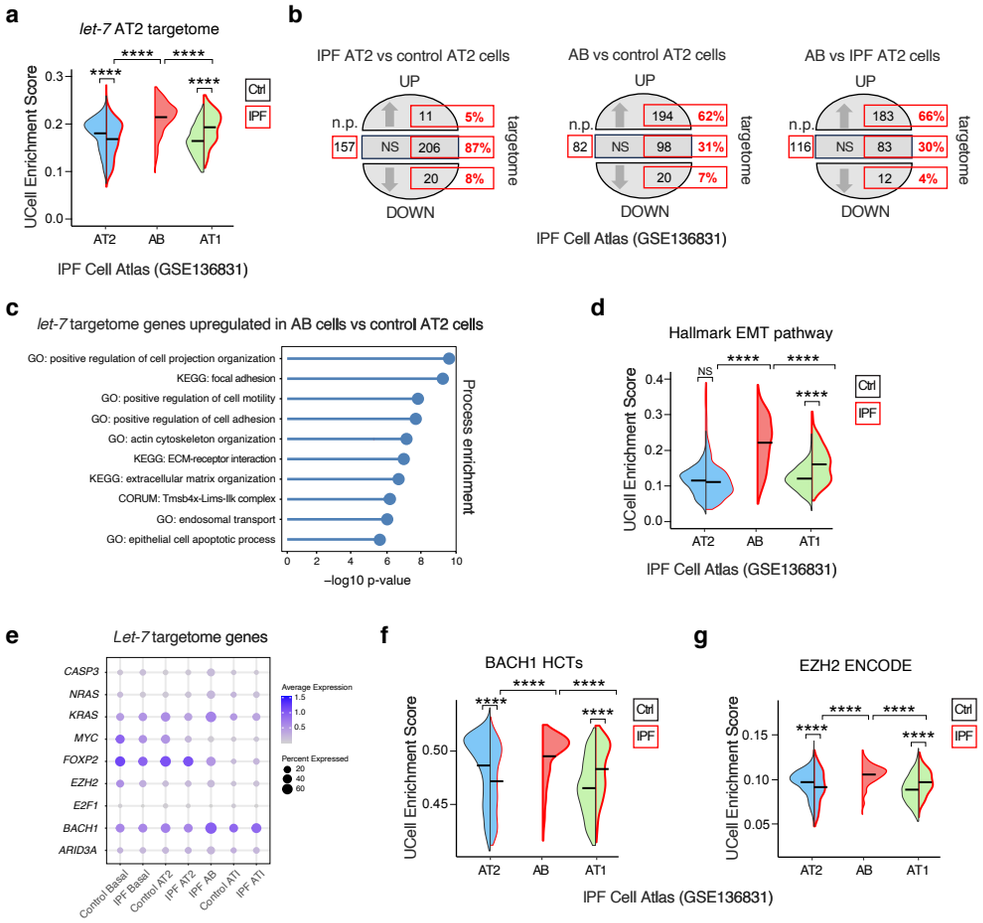

Fig 9 The *let-7* targetome is enriched in IPF "aberrant basaloid" (AB) cells. **a** UCell Enrichment scores for the murine *let-7* targetome in AT2, AB, and AT1 cells from control or IPF lungs were obtained from published scRNA-seq dataset GSE136831[14]. **b** Broken circle plots indicate the total number and proportions of *let-7* targets which are significantly upregulated (UP), downregulated (DOWN), or non significant (NS) between control (Ctrl) and IPF cells. Not present (n.p.) indicates gene targets missing in dataset GSE136831[14]. **c** Gene process enrichment analysis for upregulated *let-7* targets in AB cells compared to control AT2 cells. **d** The Hallmark EMT pathway enrichment scores in control vs IPF AT2, AB and AT1 cell samples. **e** Dot plots show the relative expression of selected *let-7* targets and identity markers in AT2, AB, and AT1 cells from control and IPF patients. **f,g** Consensus targets of BACH1 and EZH2 were evaluated for UCell Enrichment Scores in AT2, AB and AT1 cells in control and IPF patients. High confidence targets (HCT)s. **a**,**d**,**f,g** Data are mean±s.e.m half violin plots. ****$p < 0.0001$, by one way ANOVA with Sidak correction. Data was derived from published scRNA-seq dataset GSE136831[14].